

# Modeling, Design, and Control of the Rehab-Exos, a Joint Torque Controlled Upper-Limb Exoskeleton

Domenico Chiaradia\*, Massimiliano Solazzi\*, Rocco Vertechy†, and Antonio Frisoli\*

**Abstract**—This work presents a new upper-limb exoskeleton design endowed with compact elastic joints with torque sensors based on strain gauges. The torque sensor performance and the design aspects that affect unwanted non-axial moment load crosstalk are addressed in this study.

A new state-feedback interaction torque controller is proposed by modeling the multi-dof non-linear system dynamics and providing compensation of non-linear effects such as friction and gravity components. The proposed controller confers transparency to the joints.

To validate the proposed controller as well as the chosen mechanical architecture, the full-state feedback controller was compared with two other benchmark state-feedback controllers, in two tasks of the zero desired force tracking (*transparency*) and contact with a virtual stiff wall (*haptic rendering*). The *transparency* benchmarking test was performed experimentally with 10 subjects at two different reference speeds. In both experimental conditions, the proposed joint torque controller achieved higher performance, demonstrating how an active impedance by control can reach optimal performance if suitable state feedback is employed.

**Index Terms**—Joint torque sensor, elastic joint, upper limb exoskeleton, full-state feedback control, transparency, haptic rendering

## I. INTRODUCTION

Exoskeletons are robotic interfaces for human-robot interaction where the highest physical symbiosis with the human operator is achieved [1]. Unlike many industrial robots designed to exhibit a stiff structure and behavior, therefore to be used with a rigid position control, the exoskeletons are in direct contact with humans, so that they have to satisfy safety and compliance requirements common to physical Human-Robot Interaction (pHRI) devices [2].

In physical Human-Robot Interaction applications, moreover there are other performance measures inherently depending on the actuation and control that need to be considered, among which the two most relevant ones are *transparency* and *haptic rendering*:

**Transparency** relates to the ability of the robotic system interacting with a human who is moving voluntarily not to apply any assistance/ resistance to free motion [3], or equivalently means that the robot's reaction forces perceived by the user are minimal [4]. No standard procedures exist for the measurement of transparency in pHRI, but for

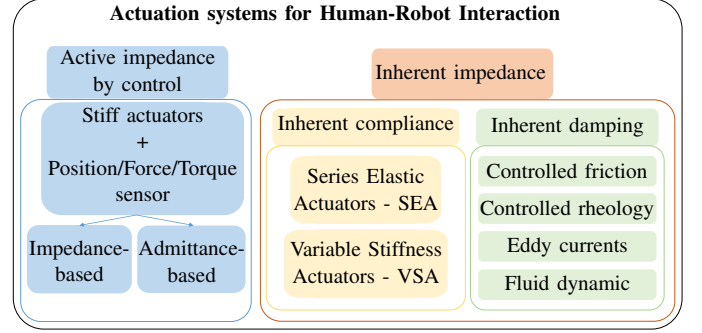


Fig. 1. Schema of variable impedance actuation systems for human-robot interaction. The impedance can be simulated and actively changed by control (this relies on position and torque sensors) or can be an inherent mechanical property of the actuator. In the latter case the mechanical stiffness can be a fixed value (SEA) or can be adjusted (VSA), and the damping can be controlled.

exoskeletons there is a general consensus to refer not only to end-effector resistance forces, but also to single joints resistance torques or measurements at contact points [4].

**Haptic rendering** refers to the capability of the device to render a desired dynamic behavior, such as a virtual impedance or a virtual wall, i.e. a task featuring both very high impedance (when in contact with the wall) and very low impedance (when out of contact) [5]. Better mechanical structures, including appropriate dimensioning of the sensors and actuators, combined with more effective control strategies should predict the maximum stiffness that can be displayed by existing devices [6].

In the last two decades, several exoskeleton solutions have been proposed using different implementation principles according to the field of application, such as neurorehabilitation and assistance [7], [8], [9], human power augmentation [10] and telepresence [11], [12], [13], where different actuation systems and technologies have been exploited, based on geared solutions [14], [15], [16], tendon drives [17], [18], hybrid solutions [19], [20], pneumatic or hydraulic actuation [21], [22].

As shown in Figure 1, the actuators found in recent exoskeletons and humanoids for pHRI can be mainly classified in two main categories, the *active impedance by control* and *inherent impedance* (compliance, damping) according to how they adjust the impedance displayed to the user, obtained either by control in the first case or as a mechanical property in the second case [23].

In *inherent compliance* actuators an electric motor is

\*D. Chiaradia, M. Solazzi and A. Frisoli are with the PERCRO Laboratory, TeCIP Institute, Scuola Superiore Sant'Anna, Pisa, Italy. E-mail: d.chiaradia@santannapisa.it.

†R. Vertechy is with the DIN-Department of Industrial Engineering University of Bologna, Bologna, Italy. E-mail: rocco.vertechy@unibo.it.

Manuscript received xxx.yy,2018; revised xxx.yy,2018

coupled with a spring with fixed (Series Elastic Actuator - SEA) or variable stiffness (Variable Stiffness Actuators - VSA), based on the principle that adding a series elastic element reduces the peak power demand to the motor. *Inherent damping* actuators are based on the control of the friction by means of eddy currents, controlled rheology or fluid dynamics.

Both SEA and VSA have been implemented in exoskeleton as for example in Lopes [24], in NEUROexos elbow exoskeleton [25] and ALTACRO locomotion exoskeleton [26].

All the variable impedance actuators have the advantage of absorbing impacts and SEA and VSA can eventually mechanically store energy during passive phases and release it in active phases of the movement cycle. VSAs generally use two motors which increases the size, weight and complexity of the actuator in comparison with an SEA [27].

On the other side, *active impedance by control* actuators are composed of electric motors coupled with a transmission/reduction system; they can be classified according to the backdrivability and sensing system. Force controlled actuators implement a force/torque sensor at the joint level and can achieve impedance behavior by closed-loop control. In general traditional actuators with no elastic or damping elements can be lighter and more compact than passive variable impedance actuators, but their time response and dynamic bandwidth is limited by control and electrical properties of actuators, such as maximum velocity of electrical motor.

Solutions based on joint torque sensor have been proposed in the last years mostly for example in lower limb exoskeletons [28], [29], [30]. The advantage of joint torque sensor based solutions is their compactness and robustness, but when the torque sensor is embedded in the joint it is sensitive to the link inertia in addition to the human interaction torques, thus affecting the system *transparency*. A mechanical solution is presented in [31] where the transparency of a lower-limb exoskeleton has been improved by positioning the force/torque sensor on the supporting cuffs, that is at the interaction point between the human leg and the exoskeleton. Sensors used to measure these deflections are generally encoders [32] and potentiometers [33]; the latter usually require custom mechanical supports to avoid errors related with its sensitivity to misalignments. While the deflection based force estimation becomes a most widely utilized method for the SEAs and VSAs and performs fidelity force control performance in various robotic applications, there are still difficulties because of the practical issues such as spring deflection measurement error or noise of the encoder signal [34]. These factors have much negative impact on SEA with high stiffness. In [35], for example, a polymer optical fiber has been mounted on the torsional spring of a SEA to read angles and torques in a more accurate way without considerably enlarging the size of the actuator at the cost of a more specific system electronics.

Thus, the adoption of inherent compliant actuation systems rather than achieving compliance by control is not a trivial choice and it depends on the desired mechanical features and is the result of a trade-off among compactness, weight, simplicity, costs, safety, efficiency. A good trade-off that prefer compactness, simplicity and uses just one motor is an active impedance by closed-loop control system that an elastic

component to transmit and to measure axial torques at the same time.

Based on the above, in this paper we introduce the design and the experimental characterization of the Rehab-Exos, an upper limb exoskeleton endowed with joint torque actuators, based on joint torque sensors and high reduction ratio, and the design of an interaction joint torque controller that maximizes both *transparency* and quality of *haptic rendering*.

In particular, to improve transparency we propose a new interaction state-feedback torque controller (JTFC1) that takes into account the multi-dof non linear system dynamics and provides a compensation of other non-linear effects, such as friction and gravity components, to achieve an accurate estimation of human interaction force. This is accomplished by a single joint optimum observer that ensures joint torque tracking, while a centralized controller estimates and compensates for the dynamics of the whole system.

To validate the proposed controller as well as the chosen mechanical architecture, the full-state feedback controller was compared with two alternative controllers, a feedback controller (JTFC2) and a passivity-based feedback controller (JTFC3), in two tasks: the zero desired force tracking (*transparency*) and the contact with a virtual stiff wall (*haptic rendering*). The *transparency* benchmarking test among the 3 controllers was performed experimentally with 10 subjects and two different reference velocities, according to the evaluation procedure already tested in [4], in order to achieve comparable benchmark results.

As far as haptic rendering, the stability behavior and quality of force rendering of the proposed controller was assessed through a virtual wall simulation implemented with increasing stiffness values and compared it with the other two benchmark controllers. In both experimental conditions, the proposed joint torque controller allows it to achieve higher performance both in term of transparency and haptic rendering, demonstrating how an active impedance by control can reach optimal performance if suitable state feedback is employed.

This paper is structured as follows: Section II presents the design of the Rehab-Exos with a particular focus on the strain gauge-based torque sensor design and issues. Section III-A provides a mathematical model of the single joint whereas in the Section III-B the full dynamics model of the Rehab-Exos is described. Section IV explains the proposed full state feedback controller and recalls two benchmark torque controllers already known in literature. Section V presents the experiments and the obtained results. Finally, discussions and conclusions are addressed in Sections VI and VII respectively.

## II. SYSTEM DESIGN

The Rehab-Exos is an active robotic exoskeleton (Fig. 2) designed with the idea to be modular, easily reconfigurable and with a good trade-off between transparency and force payload. It was conceived for rehabilitation applications and it is designed in such a way to generate controlled contact forces/torques not only at its end-effector handle, but also at intermediate contact points with the user arm. When the user is wearing the device he can control the full force interaction

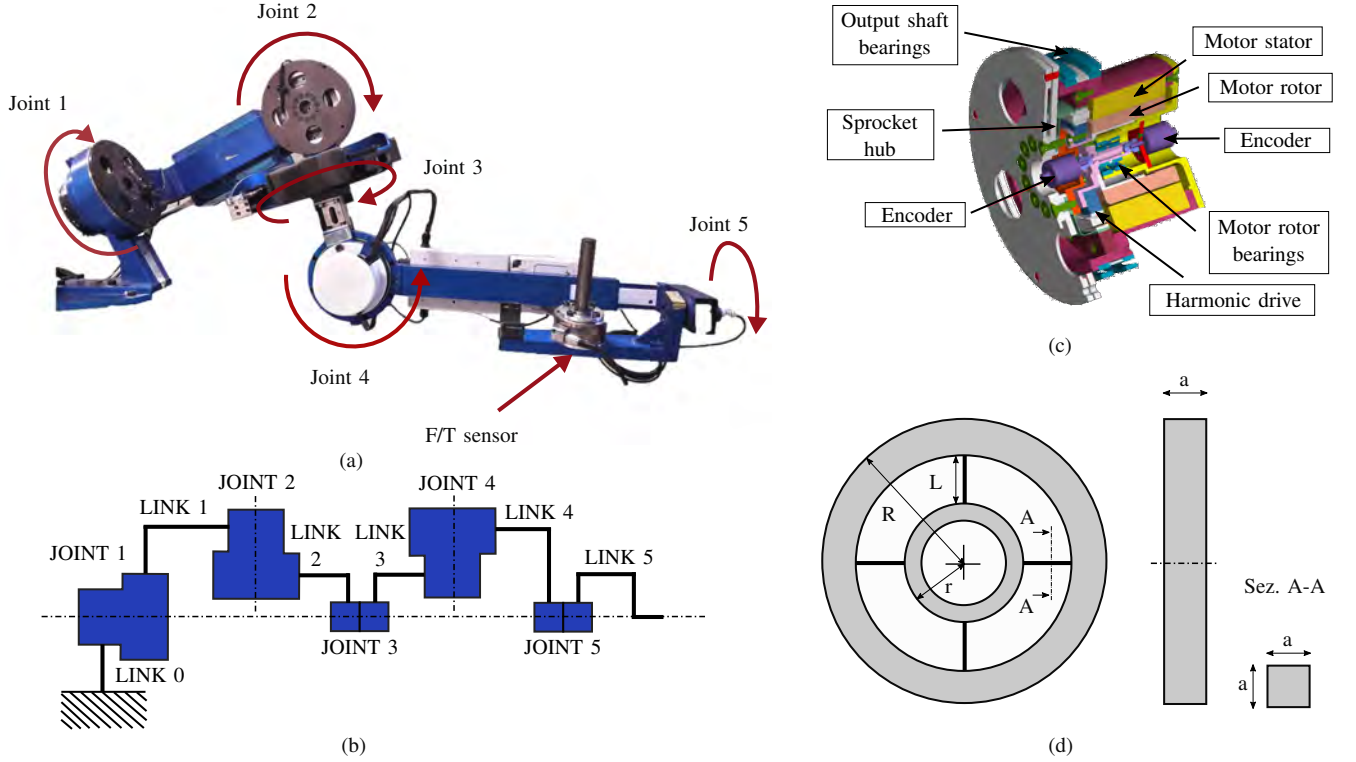


Fig. 2. (a) The Rehab-Exos. It is a 5 DOF upper-limb exoskeleton with 4 actuated joints. The joints  $J_1$ ,  $J_2$  and  $J_4$  share the same characteristics: high reduction ratio (100:1) by means of harmonic drive, embedded torque sensor and maximum actuation torque of 150 Nm. The joint  $J_3$  is composed by a semi-circular guide actuated by a DC motor through tendon transmission. Joint  $J_5$  is passive and the exoskeleton is equipped of a force/torque sensor at the end-effector that is used for evaluation purposes. (b) A schematic representation of the Rehab-Exos exoskeleton. (c) CAD section of the  $J_1$ ,  $J_2$  and  $J_4$  joint actuator of the Rehab-Exos. (d) Characteristic dimensions of the torque sensor.

with the exoskeleton and guide/be guided by shoulder and elbow) articulations of the arm. The physical interaction between user and exoskeleton is monitored by the joint torque sensors, and their performance depends on several design and implementation aspects that are addressed in subsection II-B.

#### A. Mechanical design of the Rehab-Exos

As depicted in Fig. 2, the exoskeleton has a serial architecture isomorphic with the human kinematics that comprises: a shoulder joint fixed in space and composed by three active joints  $J_1$ ,  $J_2$  and  $J_3$ ; an active elbow joint  $J_4$ ; and a passive revolute joint  $J_5$  allowing wrist pronosupination. For a more detailed description of both Rehab-Exos and actuation groups, the reader can refer to [15].

The three joints  $J_1$ ,  $J_2$  and  $J_4$  of the exoskeleton are motorized through identical actuation groups. Each joint features a custom-made frameless brushless torque motor integrating a compact Harmonic Drive (HD) component set. The actuator provides a joint output torque equal to 150 Nm with an overall weight equal to 3.7 Kg and a motor shaft inertia reduced to the joint output shaft  $J_m = 2.5 \text{ Kg m}^2$ . The Harmonic Drive performs a reduction equal to 100:1. Due to the adopted mechanical components, the joints feature limited back-drivability at motor power-off and limited mechanical complexity to ease maintenance as well as reduce costs. A CAD section of the  $J_1$ ,  $J_2$  and  $J_4$  joints is depicted in Fig. 2 c). Joint  $J_3$  is characterized by a tendon transmission that is

used to transmit the actuation torque through an open semi-circular guide. More detail on the joint  $J_3$  can be found in [15].

#### B. Design aspects of the strain gauge based torque sensor

The three joints  $J_1$ ,  $J_2$  and  $J_4$  have a torque sensor featuring a four-spoke-shape geometry. Despite further augmenting the actuation group compliance, the availability of joint-torque sensors enables multi-contact force control at multiple points distributed over the links and, additionally, makes it possible: 1) to close a stable high-bandwidth torque inner loop around each joint which is weakly affected by robot link variable inertia; 2) to suppress robot vibrations produced by the inherent transmission compliance (Harmonic Drive); 3) to reduce internal disturbance torques caused by actuator and reducer (for instance friction losses, actuator's torque ripples and gear teeth wedging actions); to measure externally applied forces/moments and complex non-linear dynamic interactions between joints and links.

The sensor consists of two fully balanced strain gauge bridges placed on different beams of the spoke, which is located at the joint output shaft. The sensor is made by AISI 630 steel, harmonic steel exhibiting yield strength of 1950 MPa, Young's modulus of 196 GPa and has been dimensioned to exhibit low weight and high sensitivity to axial moments. The axial torsional stiffness of the sensor is  $k_s = 30 \text{ kNm/rad}$

TABLE I  
CHARACTERISTIC DIMENSIONS OF THE TORQUE SENSOR

Dimension	Value [mm]
R	78
r	38
L	24
a	4
round radius	2

TABLE II  
STRAIN OF THE 4 STRAIN GAUGES

Probe 1 [m]	Probe 2 [m]	Probe 3 [m]	Probe 4 [m]
1.65e-5	-1.33e-5	-1.91e-5	2.2546e-5

and can be calculated as in (1).

$$k_s = \frac{\tau}{\theta} = \frac{Ea^4(r + L(1 - Q))}{3L^2(1/2 - Q)} \quad (1)$$

where the adimensional parameter Q is given by

$$Q = \frac{3r + L}{6r + 3L} \quad (2)$$

where, according to Fig. 2 d),  $r$  is the radius of the internal sensor ring,  $L$  is length of the beams and  $a$  is the side length of the beam section. The characteristic dimensions of the sensor are reported in TABLE I. Moreover, the overall joint torsional stiffness reduced to the joint output shaft is  $k = 11.38$  kNm/rad.

The position of the strain gauges on the beam is a trade-off: if they were positioned in the middle of the beam the sensor sensitivity would be low, on the contrary, if they were positioned near the extremities the sensor reads would be affected by the non-linearities of the rounds of the beam. The selected distance from the extremities was  $p = 1/8 L = 3$  mm. To estimate the strain of the beam in a given point with distance  $p$  from the inner ring under a certain axial torque  $\tau$ , the normal tension  $\sigma_p$  that acts on that point  $p$  needs to be computed as

$$\sigma_p = \frac{3\tau((1 - Q)L - p)}{2a^3((1 - Q)L + r)} \quad (3)$$

and then the strain follow as

$$\epsilon_A = \frac{\sigma}{E} \quad (4)$$

where  $E$  is the Young's modulus.

Theoretically, i.e. using (4), at 3 mm from the inner ring and under an axial torque of 120 Nm, a maximum strain of  $2.7 \times 10^{-3}$  m is obtained. The same test has been conducted using a FEM software tool (Ansys®) because the surface of the strain gauge is not negligible compared to the beam one (see Fig. 3) obtaining a maximum strain of  $1.98 \times 10^{-3}$  m. The strain of each strain gauge when a 1Nm load is applied can be shown in TABLE II.

An important characteristic of the torque sensor is the sensitivity to non-axial moments, thus an experimental test has been conducted to compute the sensitivity, i.e. a predetermined non-axial torque has been exerted on the sensor in 4 configurations

TABLE III  
SENSOR READS TO NON-AXIAL MOMENTS

Applied Torque [Nm]	Sensor reads per angle [Nm]			
	0°	45°	90°	180°
32	1.6	2.4	2.2	2.3
64	2.9	4.8	4.4	4.4
96	4.5	7.5	6.9	6.9

(angle) of the sensor. Experimental results are reported in TABLE III and the sensitivity is equal to

$$S_S = \frac{C_{mis}}{C_S} = 0.067 \quad (5)$$

The sensitivity to non-axial moments is relatively high compared to one mentioned in [36].

The reason of these results has been investigated and two causes (or a combination of them) have been proposed. The first cause of error could be a strain gauge mounting misalignment. The second cause could be an excessive deformation of the sensor due to the non-axial moments. About the first hypothesis, the sensitivity of the strain gauges to non-axial load  $C_S$  (when a flexible model of the HD is considered) due to strain gauge misalignment can be modeled as

$$S_{misal} = k_s \cdot (k_{ex} \cdot e_x + k_{e\theta} \cdot e_\theta) \quad (6)$$

where  $k_s$  is a scaling factor equal to  $7.87e^{-3}$ ,  $k_{ex}$  is the sensitivity to linear mounting misalignment equal to 3,  $k_{e\theta}$  is the sensitivity to angular mounting misalignment equal to 2.3, whereas  $e_x$  and  $e_\theta$  are the positional and angular misalignment errors respectively (see Fig. 3 a)). Equation (6) and the measured sensitivity of 0.067 lead to a misalignment error of millimeters and decades of degree, but these values are over the actual misalignment the installation operator may have introduced as it can be seen in Fig. 3 b).

About the second hypothesis it is worth to notice that the sensor from a structural point of view is in series to the HD and these are in parallel with a couple of bearings. This parallel chain composes a hyper-static system (see Fig. 4), therefore the excessive sensitivity may be due to mounting misalignment of the mechanical parts of the chain.

For the study of the hyper-static system a linear elastic behavior of the system parts were supposed and the system response at non-axial moments was modeled as a mono-dimensional model. The overall joint stiffness to non-axial moments  $K_{TOT}$  was experimentally evaluated, whereas the non-axial moment stiffness of the torque sensor  $K_{TS}$  and of the HD  $K_{HD}$  were computed via FEM analysis. The FEM results are depicted in Fig. 3 and the stiffness values are reported in table TABLE IV.

A possible mounting misalignment of the hyper-static chain may be a collinear and/or concentric mounting misalignment between the sensor axis and the bearing axis. In this case, the HD works as an universal joint that connect the sensor (that is connected to the n+1 link ) and the n-th link. The sensitivity to non-axial moments defined in equation (5) and the mechanical properties in TABLE IV lead to a theoretical

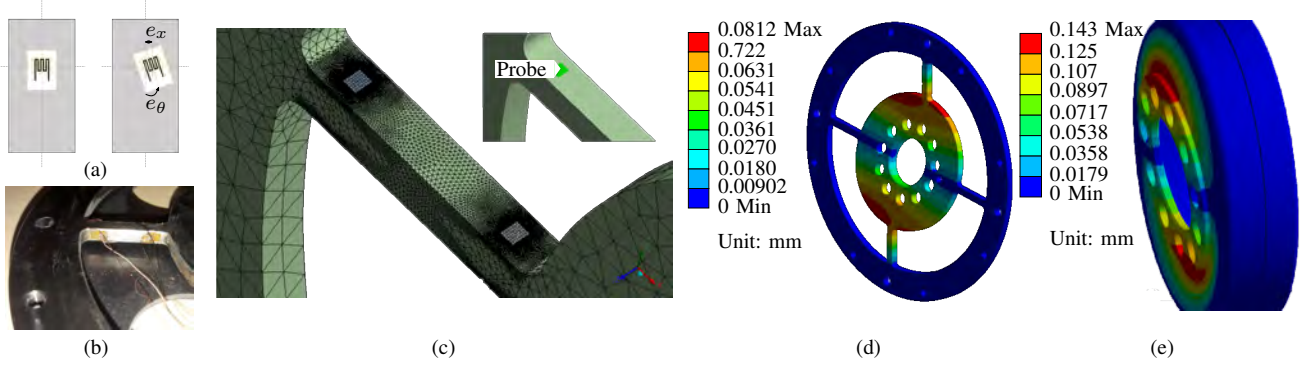


Fig. 3. (a) A possible cause of high sensitivity to non-axial load is the strain gauges's mounting misalignment.  $e_x$  is the linear displacement and the angular one is  $e_\theta$  are highlighted. (b) A detail of the mounted strain gauges on the torque sensor. (c) For the FEM analysis a more dense grid mesh for the zone of interest has been used. For each area the average strain along the radial direction has been computed. (d) The FEM analysis results of the torque sensor, and of the flexible spline deformation under non-axial load (e).

TABLE IV  
STIFFNESS OF THE COMPONENTS

Component	Stiffness [kNm/rad]
$K_{TS}$	4.1
$K_{HD}$	0.4
$K_B$	23.6
$K_{TOT}$	24

mounting misalignment of about  $0.5 \text{ mm}$ , but this value is not in agreement with the design tolerances and components data-sheets from which a misalignment of about  $0.05 \text{ mm}$  results in the worst case.

To summarize, unwanted sensor reads to non-axial load may be due to the combination of effects from sensor mounting misalignments and HD excessive deformation.

In order to minimize this undesired effect, we adopted a model-free adaptive method based on artificial neural networks (ANN) to characterize and compensate this non-linear response of the sensors, in alternative to modeling approaches in reason of the complexity of the phenomenon. Considering the ideal and linear response of the sensor, the torque readings can be expressed as  $\tau_s = k_v * v$ , where  $v$  is the measured voltage tension and  $k_v$  is the torque sensor's voltage constant. In the real case it can be written  $\hat{\tau}_s = k_v * v + \delta\tau$ , where  $\delta\tau$  is the non-linear influence on the sensor readings due to the mounting and non-axial loads. By experimental evidence, it's possible to assert that the term  $\delta\tau$  varies in a non-linear way with respect to the exoskeleton pose (joint angles) and load.

The mounting errors influence the torque readings non-linearly with respect to the joint angle, while the non-axial torques depend in part on the interaction with the human and in part on the dynamics and gravitational torques acting on the considered joint. For all three sensors, the  $k_v$  constants have been experimentally evaluated. In order to minimize the effect of non-linear undesired term  $\delta\tau$ , an ANN has been used. An ANN is a mathematical approximation approach that can infer non-linear behavior from experimental acquisitions. The ANN with 7 neurons in the hidden layer and sigmoid activation function are employed to estimate the error on the basis of

the 4 angles and load on each axis. The angular information is useful to infer the assembly error component, whereas for the load influence the gravitational torque has been used.

To train the neural network the whole workspace has been partitioned in 414 target points. The torque sensor readings were acquired while the exoskeleton was holding the target position. For each joint, the training has been done using as input the 4 angles and the gravity torque that act on the joint (computed by model), and as output the residual value  $\delta\tau = G_i(\theta_m) - k_v * v$ , where  $G_i$  is the gravity load on the  $i$ -th joint when the pose is given by the angle vector  $\theta_m$ . The set of target points was divided in 3 parts: 70% for the training set, 20% for the validation set and 10% for the test set. The regression value between the ANN output and the target points is 0.99. The actual sensor torque estimation is given by  $\hat{\tau}_s = k_v * v + \delta\tau(\theta_m, G_i)$ .

### C. Control Hardware

The control architecture of the Rehab-Exos is decentralized and based on the EtherCAT communication bus in order to guarantee both optimal signal to noise ratio in the acquisition of analogical signals, i.e. force sensors, and higher standards of safety. The EtherCAT communication network consists of one master controller and four Ethercat Slave Controllers (ESC), one for each actuation joint. The master controller is handled by Simulink Real-Time™ Operating System that executes the centralized control model at  $2 \text{ kHz}$  frequency.

Motors of the exoskeleton consist of three  $170 \text{ VDC}$  power supplied brushless motors on the 1st, 2nd, and 4th joint each one driven by programmable current drivers and one  $48 \text{ VDC}$  power supplied DC motor on the 3rd joint. All of them are provided with one incremental encoder and one torque sensor.

Each ESC board is a custom control board featuring an up to  $72 \text{ Mhz}$  ARM7 micro-controller, 4 14-bit DAC output interfaces (to set the reference of the current drives), 10 14-bit Analog-to-Digital Converter (ADC) channels (to acquire the torque signals through 2 Wheatstone full-bridge channels that are pre-amplified) and the EtherCAT ET1100 controller linking to double-port Ethernet interface.



### III. DYNAMIC MODEL

#### A. Single joint model

The joints of the exoskeleton can be modeled with a lumped parameter model due to the elasticity of the harmonic drive speed reducer and torque sensor (for joints 1, 2 and 4) and of tendon transmission for joint 3. The used single joint model is a 2-mass with spring and damper (Fig. 5).

The single joint dynamics is formulated by the following equations:

$$\begin{aligned} I_{m,i}\ddot{\theta}_{m,i} + c_{m,i}\dot{\theta}_{m,i} + c_{t,i}(\dot{\theta}_{m,i} - \dot{\theta}_i) + k_{t,i}(\theta_{m,i} - \theta_i) &= \tau_{m,i} + \tau_{d,i} \\ I_{l,i}\ddot{\theta}_i + c_{t,i}(\dot{\theta}_i - \dot{\theta}_{m,i}) + k_{t,i}(\theta_i - \theta_{m,i}) &= \tau_{l,i} \end{aligned} \quad (7)$$

where referring to the  $i$ -th joint,  $\theta_{m,i}$  and  $\theta_i$  stand for motor and joint angles respectively,  $k_{t,i}$  and  $c_{t,i}$  are the stiffness and viscous coefficient of the transmission, that were experimentally characterized.  $I_{m,i}$  is motor inertia,  $I_{l,i}$  is average link inertia considered as constant,  $\tau_{m,i}$  is the motor torque,  $\tau_{d,i}$  is a disturbance torque acting on the motor rotor which accounts for internal friction and ripple effects of both motor and harmonic drive, while  $\tau_{l,i}$  is the external torque acting directly on the output link. The  $\tau_{l,i}$  torque accounts for the exogenous input due to the interaction with the human, and endogenous input accounting for unmodeled non-linear effects, such as dynamic or gravity forces.

1) *Experimental characterization of single joint performance:* As described in II-A the joint is equipped with a torque sensor that is a part of the transmission chain and is capable of measuring the elastic torque  $\tau_{s,i}$ , which acts between motor rotor and joint output link. The elastic sensor torque can be expressed by  $\tau_{s,i} = k_{t,i}(\theta_i - \theta_{m,i})$ . The joint dynamics can be re-written expliciting the  $\tau_{s,i}$  readings starting from  $\tau_{s,i}$  definition, its 1st and 2nd derivatives and using the equations 7. It is obtained:

$$\ddot{\tau}_{s,i} + \frac{c_{t,i}}{I_i}\dot{\tau}_{s,i} + \frac{k_{t,i}}{I_i}\tau_{s,i} = \frac{k_{t,i}}{I_{l,i}}\tau_l + \frac{k_{t,i}}{I_{l,i}}\tau_g - \frac{k_{t,i}}{I_{m,i}}\tau_d - \frac{k_{t,i}}{I_{m,i}}\tau_m \quad (8)$$

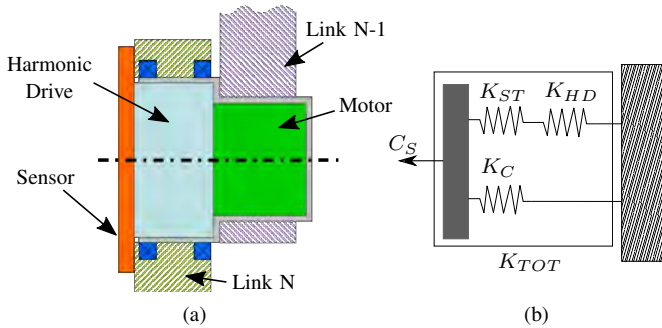


Fig. 4. (a) The schematic representation of the joint. The torque sensor is a series elastic element between the motor and the link  $n$ . The torque sensor is not structural and has been designed to transmit only axial torque. (b) The kinematic chain of the joint to non-axial loads.  $K_{TS}$  and  $K_{HD}$  are the stiffness of the torque sensor and of the Harmonic Drive to non-axial load respectively, whereas  $K_B$  is the bearing stiffness.

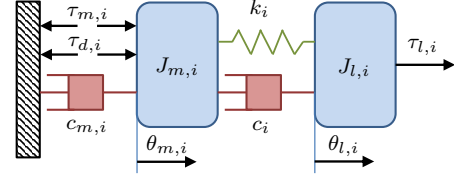


Fig. 5. The 2-mass model for each joint.

TABLE V  
THE NATURAL FREQUENCY OF THE JOINTS

Joint	Avg. link inertia [ $\text{Kg/m}^2$ ]	Natural freq. [ $\text{Hz}$ ]
1	0.9639	19.3930
2	1.11	18.3501
4	0.1925	39.6797

where  $I_i = I_l I_m / (I_l + I_m)$ . The natural frequency of this system is  $\omega_n = \sqrt{k_{t,i}/I_i}/2\pi$ . The natural frequency has been experimentally evaluated for a single joint in a test-rig analyzing the response of the  $\tau_s$  when a chirp command is used for the  $\tau_m$  motor torque.

From Fig. 6, use of the Half-Power Bandwidth method returns  $c = 11.8 \text{ Nms/rad}$  as the overall damping coefficient of the flexible joint (this value has also been validated via the Logarithmic Decrement method). Considering the exoskeleton,

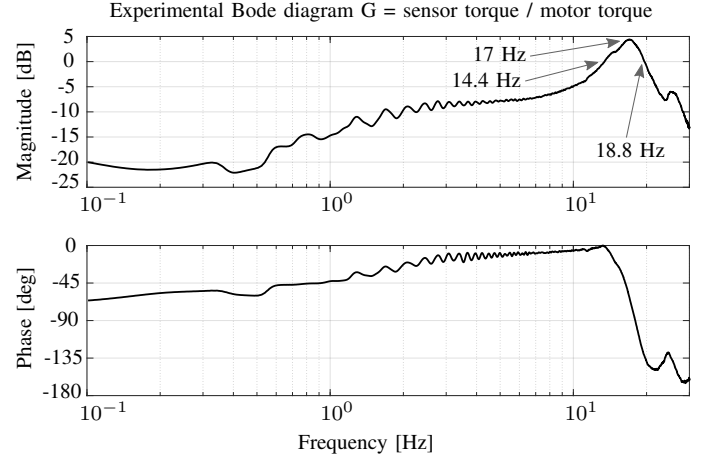


Fig. 6. Experimental open-loop response (Bode magnitude plot) of joints 1, 2 and 4: joint sensor torque vs. motor torque command in standardized testbed conditions.

every joint sees a link inertia that depends on the pose so the natural frequency of each joint depends on the pose of the exoskeleton. Considering an average link inertia, it can be obtained the natural frequency for each joint elastic transmission. Results are shown in the TABLE V. For all these three joints the motor inertia is the same and it is equivalent to  $3.742 \text{ Kg/m}^2$ .

#### B. Multiple joints model

Given the single joint two-mass model, the dynamic model of the whole exoskeleton can be formulated in matrix form as follows:

$$\begin{aligned}
& \underbrace{\mathbf{I}_m \mathbf{D} \ddot{\boldsymbol{\theta}}_m + \mathbf{B}_m \mathbf{D} \dot{\boldsymbol{\theta}}_m}_{\tau_m + \tau_d} + \underbrace{\mathbf{C}_t (\mathbf{D} \dot{\boldsymbol{\theta}}_m - \dot{\boldsymbol{\theta}}) + \mathbf{K}_t (\mathbf{D} \boldsymbol{\theta}_m - \boldsymbol{\theta})}_{\text{Elastic transmission torque}} \\
& \underbrace{\mathbf{M}(\boldsymbol{\theta}) \ddot{\boldsymbol{\theta}} + \mathbf{C}(\dot{\boldsymbol{\theta}}, \boldsymbol{\theta}) \dot{\boldsymbol{\theta}}}_{\text{Joint dynamics}} + \underbrace{\mathbf{C}_t (\dot{\boldsymbol{\theta}} - \mathbf{D} \dot{\boldsymbol{\theta}}_m) + \mathbf{K}_t (\boldsymbol{\theta} - \mathbf{D} \boldsymbol{\theta}_m)}_{\text{Elastic transmission torque}} + \mathbf{G}(\boldsymbol{\theta}) = \mathbf{J}^T \mathbf{F}_h
\end{aligned} \quad (9)$$

where  $\mathbf{I}_m$ ,  $\mathbf{B}_m$ ,  $\mathbf{D}$ ,  $\mathbf{K}_t$  and  $\mathbf{C}_t$  are diagonal matrices.  $\mathbf{I}_m$  and  $\mathbf{B}_m$  model inertia and viscous friction at motor respectively, while  $\mathbf{K}_t$  and  $\mathbf{C}_t$  model stiffness and damping associated with the elastic transmission and  $\mathbf{D}$  models the transmission reduction factor introduced by joint gearheads;  $\mathbf{G}$  models the effects of gravity force on links;  $\mathbf{F}_h$  are the external forces acting on the system due to human interaction and the respective joint torques are computed by multiplying them by the transposed Jacobian matrix  $\mathbf{J}^T$  evaluated in the actual exoskeleton configuration. The multi-joint model introduces cross-coupling among joints and non-linearities, with terms  $\mathbf{C}(\dot{\boldsymbol{\theta}}, \boldsymbol{\theta})$  that models Coriolis effects and  $\mathbf{M}(\boldsymbol{\theta})$  that represents link inertias and that can be decomposed into a diagonal constant component and a variable component as follows:

$$\mathbf{M} \ddot{\boldsymbol{\theta}} = \underbrace{\bar{\mathbf{M}} \ddot{\boldsymbol{\theta}}}_{\text{constant}} + \underbrace{\Delta \mathbf{M}(\boldsymbol{\theta}) \ddot{\boldsymbol{\theta}}}_{\text{variable}} \quad (10)$$

By making a replacement of variables introducing this expression for the joint torque

$$\boldsymbol{\tau}_s = -\mathbf{K}_t (\mathbf{D} \boldsymbol{\theta}_m - \boldsymbol{\theta}) \quad (11)$$

the dynamics equations (9) can be reformulated as follows in terms of new variables  $\boldsymbol{\tau}_s$  and  $\boldsymbol{\theta}_m$ :

$$\begin{cases} \mathbf{I}_m \mathbf{D} \ddot{\boldsymbol{\theta}}_m + \mathbf{B}_m \mathbf{D} \dot{\boldsymbol{\theta}}_m = \mathbf{K}_t^{-1} \mathbf{C}_t \dot{\boldsymbol{\tau}}_s + \boldsymbol{\tau}_s + \boldsymbol{\tau}_d + \mathbf{u} \\ \ddot{\boldsymbol{\tau}}_s + \mathbf{C}_t \mathbf{I}_i^{-1} \dot{\boldsymbol{\tau}}_s + \mathbf{K}_t \mathbf{I}_i^{-1} \boldsymbol{\tau}_s = \mathbf{K}_t \mathbf{I}_m^{-1} (\mathbf{I}_m \bar{\mathbf{M}}^{-1} \mathbf{J}^T \mathbf{F}_l + \mathbf{B}_m \mathbf{D} \dot{\boldsymbol{\theta}}_m - \boldsymbol{\tau}_d - \mathbf{u}) \end{cases} \quad (12)$$

where  $\mathbf{u}$  (see appendix) represents the actual control command and the external disturbance forces have been collected within the external load force  $\mathbf{F}_l$  term (see Appendix I for detailed derivation of terms).

This form of the dynamics equation is useful for defining a full-state feedback control law and an optimal observer for the estimation of joint torque.

1) *Joint acceleration estimation:* The full dynamics model of the exoskeleton is dependent on the acceleration of each joint. In order to estimate and compensate for the dynamics of the device, an observer for the joint acceleration has been designed. The observer estimates the acceleration from motor encoder  $\theta_{m,i}$ , joint torque  $\tau_{s,i}$  and the imposed control torque  $\tau_{m,i}$ .  $\tau_{s,i}$  is the torque measured by the sensor at the joint and can be expressed as in equation (11).

The acceleration can be estimated starting from a model of the actuation group (motor and gearhead), in particular by modeling the torque acting on the actuation group as  $\tau_{m,i} - \tau_{s,i}$  and by considering the losses as a static and a velocity-dependent viscous friction. Thus, the acceleration can be estimated as:

$$\begin{cases} \ddot{\theta}_{m,i} = 0 & \text{for } -\tau_{A,i} < \tau_{m,i} - \tau_{s,i} < \tau_{A,i} \\ \ddot{\theta}_{m,i} = \frac{\tau_{m,i} - \tau_{s,i} - c_{m,i} \dot{\theta}_{m,i}}{J_{m,i}} & \text{otherwise} \end{cases} \quad (13)$$

where  $\tau_{A,i}$  is the static friction torque and  $c_{m,i}$  is the dynamic friction coefficient that were experimentally evaluated. The torque saturation effects due to power supply voltage limits are modeled as:

$$k_c \frac{-V_{max} - k_v \dot{\theta}_{m,i}}{R} < \tau_{m,i} < k_c \frac{V_{max} - k_v \dot{\theta}_{m,i}}{R} \quad (14)$$

depending on the electric constants of each motor, and in particular where  $k_c$  is the associated torque constant,  $k_v$  is the velocity constant,  $R$  is the winding terminal resistance and  $V_{max}$  is the maximum supply voltage to the motor. An optimum observer has been used to estimate the acceleration term  $\ddot{\theta}_{m,i}$  and a diagram of the estimation of acceleration by using control and measured torques is shown in Fig. 7.

The model can be expressed in the state variable form as follows:

$$\begin{cases} \dot{\mathbf{x}} = \mathbf{A} \mathbf{x} + \Gamma \mathbf{d} \\ \mathbf{y} = \mathbf{C} \mathbf{x} \end{cases} \quad (15)$$

where

$$\mathbf{x} = \begin{bmatrix} \theta_{m,i} \\ \dot{\theta}_{m,i} \\ \ddot{\theta}_{m,i} \end{bmatrix} \quad \mathbf{A} = \begin{pmatrix} 0 & 1 & 0 \\ 0 & 0 & 1 \\ 0 & 0 & 0 \end{pmatrix} \quad \Gamma = \begin{bmatrix} 0 \\ 0 \\ 1 \end{bmatrix} \quad \mathbf{C} = \begin{pmatrix} 1 & 0 & 0 \\ 0 & 0 & 1 \end{pmatrix} \quad (16)$$

and  $\mathbf{d}$  is the process noise.

The observer can be formulated as:

$$\dot{\hat{\mathbf{x}}} = \mathbf{A} \hat{\mathbf{x}} + \mathbf{L} (\mathbf{y} - \mathbf{C} \hat{\mathbf{x}}) \quad (17)$$

where  $\mathbf{L}$  is the gain matrix of the observer. A scheme of the observer is depicted in figure 7.

The gain  $\mathbf{L}$  was found resolving the problem of a Kalman optimum observer based on the experimental covariance data of measurement and process noise. Measurement noise was derived from motor encoder  $\theta_{m,i}$  measurements, that mainly takes into account the encoder quantization and motor acceleration  $\ddot{\theta}_{m,i}$  estimation through (13), thanks to the available torque measurement.

optimum observer Lueberger where the gain  $\mathbf{L}$  has been tuned based on experimentally measured covariances on  $\theta_m$  and  $\mathbf{R}$  measurement noise, process disturbance. As an example, the comparison between the real-time estimated acceleration (gray dotted line) and the off-line calculated acceleration (black solid line) for the first two joints is shown in figure 8.

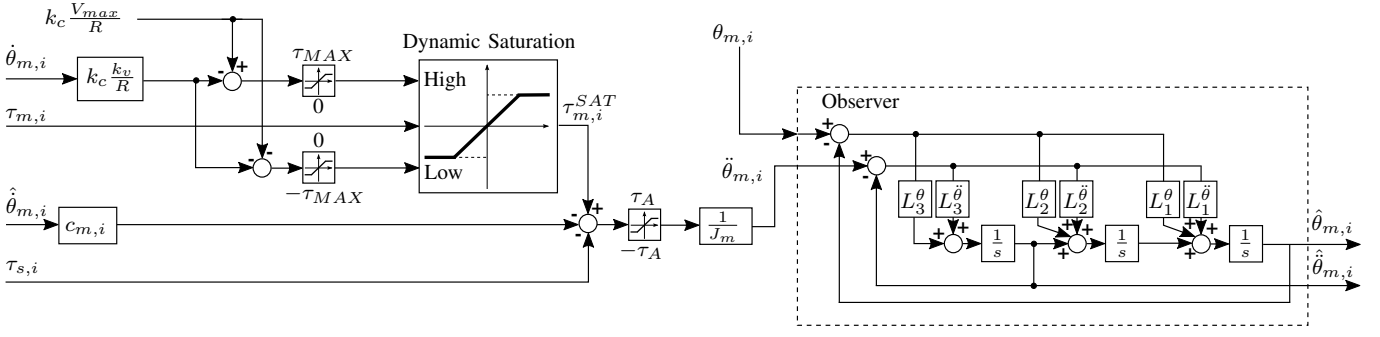


Fig. 7. Estimation scheme of the acceleration from torque measurement. The left side of the scheme models the motor dynamics and it considers saturation effects. The right side shows the implementation scheme of the observer.

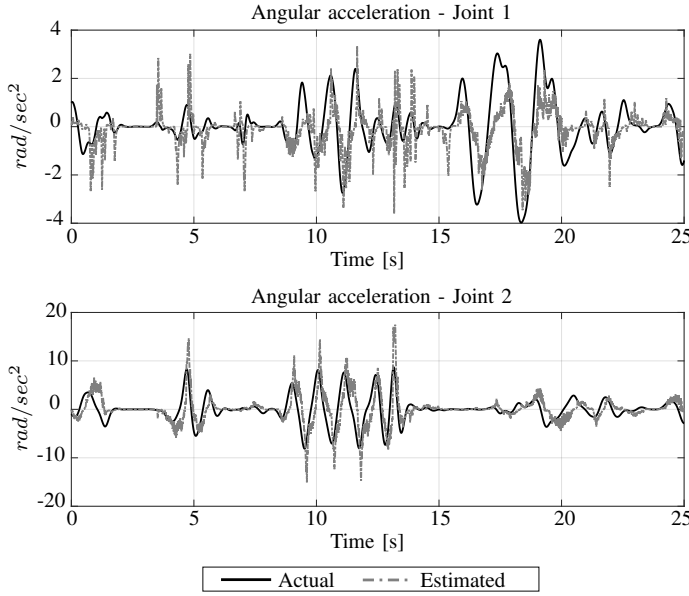


Fig. 8. Comparison between the estimated (gray dashed line) and actual (solid black line) joint acceleration (joint 1 and 2 are chosen for reference only and similar results was obtained for all the joints).

2) *Dynamics compensation*: As reported by equation (32), the torques measured by joint sensors are due to the human force and any load applied on the links ( $F_l$ ). To have a good estimation of human forces by torque sensors, it is necessary to remove from torque measurements the gravity and dynamics loads applied to the links. The gravity contribution depends only on the pose of the exoskeleton and it can be calculated by the position signals provided by the motor encoders. The gravitational term is already compensated in feed-forward by the term  $\hat{G}(D\hat{\theta}_m)$  in  $\tau_m$ , except for the term  $\delta g$ . On the other side, the dynamics contribution depends both on the pose and the acceleration and velocity of the links, which are not directly provided by any sensor, but are provided in first approximation as  $D\hat{\ddot{\theta}}_m$  by the observer described in section III-B1.

The dynamic torques due to the link inertias and measured by the joint torque sensors can be so estimated as the sum of the inertial contribution and the Coriolis effect:

$$\hat{\tau}_{dyn} \approx \hat{M}(D\theta_m)D\ddot{\theta}_m + \hat{C}(D\theta_m, D\dot{\theta}_m)D\dot{\theta}_m \quad (18)$$

where matrices  $\hat{M}$  and  $\hat{C}$  are calculated taking into account for each joint the inertia of the parts supported by the torque sensor, discarding the inertia of the actuator of the joint.

The estimated dynamic torques are then used to compensate the dynamic effects of the link: the compensation torques  $\alpha\hat{\tau}_{dyn}$ , with  $0 < \alpha < 1$ , are a percentage of the estimated torques  $\hat{\tau}_{dyn}$ . The compensation torques are added to the desired torques  $\tau_s^D$  as input to the state feedback controller and feed-back with the estimated torque  $\hat{\tau}_s$ .

#### IV. FULL STATE, BASIC AND PASSIVITY-BASED FEEDBACK CONTROLLERS

From the full dynamic model of the exoskeleton, a novel full state feedback control law was derived and implemented. This control law is identified in the following with the acronym JTFC1 and explained in subsection IV-B. To implement the control, the state of the system and, more in particular, the joint torque was estimated through a Kalman Filter described in subsection IV-A. To evaluate the performance of the proposed full state feedback control, two other torque controls inspired to existing joint torque controls available in literature have been implemented, identified respectively with the acronyms JTFC2 and JTFC3.

The JTFC2, presented in subsection IV-C, is based on a torque control for single joint based on torque sensor first introduced by Hashimoto [37]. In order to compare the basic torque control with our full state feedback control, the Hashimoto formulation was extended and generalized to a multi-dof case.

The JTFC3, reported in subsection IV-D, was inspired to the passivity-based control law [38] implemented for the DLR Light Weight Robot III (LWR III) that guarantees the passivity of the controlled system. The DLR LWR III shows a joint design compatible with the Rehab-Exos one, since both systems make use of the joint torque sensor to estimate the interaction torques/forces with the environment/human.

##### A. An optimal observer for estimation of joint torque

Since the correct state estimation is essential for the design of a full-state feedback joint-torque controller, the knowledge



of the interaction torques between the human arm and the exoskeleton are required for torque control implementation. The joint torque sensor provides a raw measurement  $\tau_{s,i}$  that can be used together with the measured joint position  $\theta_{m,i}$  to filter the sensed torque and to estimate the full system state, given by  $[\tau_{s,i}, \dot{\tau}_{s,i}, \theta_{m,i}, \dot{\theta}_{m,i}, \tau_{d,i}, \tau_{l,i}]$ , where  $\tau_l = \mathbf{J}^T \mathbf{F}_l$ . Thus, a full-state Kalman filter has been designed to clean out both  $\theta_{m,i}$  from quantization noise  $w_{\theta,i}$  and  $\tau_{s,i}$  from measurement noise  $w_{\tau,i}$ , as well as to estimate the remaining variables.

Following [39], the dynamics of the two state components  $\tau_{d,i}$  and  $\tau_{l,i}$  can be modeled as two distinct Wiener processes (i.e. as two distinct non-stationary random processes)  $\dot{\tau}_{d,i} = v_{d,i}$  and  $\dot{\tau}_{l,i} = v_{l,i}$ . Starting from equation (37) the following meta-system can be derived:

$$\begin{cases} \dot{\tau}_i = \mathbf{A}_i \tau_i + \mathbf{B}_i \tau_{m,i} + \Gamma v_i \\ y_i = \mathbf{C} \tau_i + w_i \end{cases} \quad (19)$$

where  $\tau_i^T = [\dot{\tau}_{s,i} \ \tau_{s,i} \ \dot{\theta}_{m,i} \ \theta_{m,i} \ \tau_{l,i} \ \tau_{d,i}]$  is the meta-state vector,  $v_i^T = [v_{l,i} \ v_{d,i}]$  is the vector of process noises with variances  $V_{l,i}$  and  $V_{d,i}$ ,  $w_i^T = [w_{\tau,i} \ w_{\theta,i}]$  is the vector of measurement noises with variances  $W_{l,i}$  and  $W_{d,i}$ , whereas:

$$\mathbf{A}_i = \begin{pmatrix} \frac{-c_{t,i}}{J_i} & \frac{-k_{t,i}}{J_i} & \frac{k_{t,i} b_{m,i}}{J_{m,i}} & 0 & \frac{k_{t,i}}{J_{l,i}} & \frac{-k_{t,i}}{J_{m,i}} \\ 1 & 0 & 0 & 0 & 0 & 0 \\ \frac{c_{t,i}}{k_{t,i} J_{m,i}} & \frac{1}{J_{m,i}} & \frac{-b_{m,i}}{J_{m,i}} & 0 & 0 & \frac{1}{J_{m,i}} \\ 0 & 0 & 1 & 0 & 0 & 0 \\ 0 & 0 & 0 & 0 & 0 & 0 \\ 0 & 0 & 0 & 0 & 0 & 0 \end{pmatrix} \quad (20)$$

$$\mathbf{B}_i = \begin{bmatrix} \frac{-k_{t,i}}{J_{m,i}} \\ 0 \\ \frac{1}{J_{m,i}} \\ 0 \\ 0 \\ 0 \end{bmatrix} \quad \Gamma = \begin{pmatrix} 0 & 0 \\ 0 & 0 \\ 0 & 0 \\ 1 & 0 \\ 0 & 1 \end{pmatrix} \quad \mathbf{C} = \begin{pmatrix} 0 & 0 \\ 1 & 0 \\ 0 & 0 \\ 0 & 1 \\ 0 & 0 \\ 0 & 0 \end{pmatrix}$$

### B. A full state feedback controller (JTFC1)

The proposed control law is based on the full state obtained from the state observer described by (19) (20), where the input control  $\mathbf{u}$  is splitted up into one term  $\mathbf{u}_f$ , which implement control force behavior, and another term  $\mathbf{u}_g$ , which acts as a gravity compensation

$$\mathbf{u} = \mathbf{u}_f + \mathbf{u}_g \quad (21)$$

The two above terms are expressed as:

$$\mathbf{u}_g = \mathbf{G}(\mathbf{D} \hat{\theta}_m) \quad (22)$$

$$\mathbf{u}_f = - \underbrace{\mathbf{I}_i^{-1} \mathbf{I}_m \tau_s^D}_{\text{desired torque}} - \underbrace{\mathbf{I}_m \mathbf{K}_t^{-1} (\ddot{\tau}_s^D - \mathbf{K}_d \dot{e} - \mathbf{K}_p e)}_{\text{state feedback}} + \underbrace{(\mathbf{I}_m \bar{\mathbf{M}}^{-1} \mathbf{J}^T \hat{\mathbf{F}}_l + \mathbf{B}_m \mathbf{D} \dot{\theta}_m - \hat{\tau}_d)}_{\text{unmodeled dynamics compensation}} \quad (23)$$

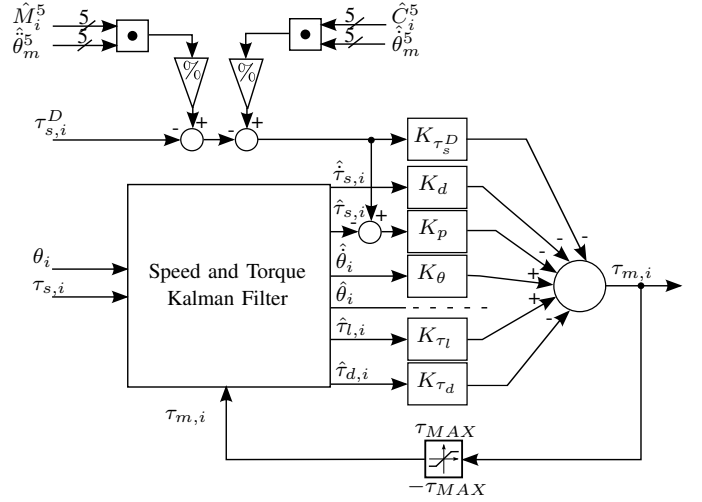


Fig. 9. The scheme of the full state control feedback with the dynamic compensation. Inertial and Coriolis effects make use of the estimated joint accelerations and velocities (see scheme of Fig. 7).

where  $e = \tau_s - \tau_s^D$  is the error on sensor torque, given the desired sensor torque  $\tau_s^D$ . Let us assume moreover that

$$\begin{cases} \dot{\tau}_s^D = 0 & \text{so } \dot{e} = \dot{\tau}_s, \\ \ddot{\tau}_s^D = 0 & \text{so } \ddot{e} = \ddot{\tau}_s. \end{cases} \quad (24)$$

The modified dynamics with the control laws (21), (22) and (23), leads to a stable error dynamics equations:

$$0 = \ddot{e} + (\mathbf{C}_t \mathbf{I}_i^{-1} + \mathbf{K}_d) \dot{e} + (\mathbf{K}_t \mathbf{I}_i^{-1} + \mathbf{K}_p) e \quad (25)$$

The convergence of error  $e$  to zero can so be adjusted by choosing the proportional and derivative gains  $\mathbf{K}_p$  and  $\mathbf{K}_d$ , to obtain the desired dynamic response.

Based on the above, from the double derivation of (11), we obtain the dynamics

$$\ddot{\theta}_m = \mathbf{D}^{-1} (\ddot{\theta} - \mathbf{K}_t^{-1} \ddot{e}) \quad (26)$$

Figure 9 reports the schema of the proposed full state feedback control that takes into account the dynamic compensation contributes. Note that the torque sensor reads  $\tau_{s,i}$  and the commanded motor torques  $\tau_{m,i}$  are net of the gravity compensation term  $u_g$ .

### C. A basic state feedback controller (JTFC2)

The basic state feedback controller is derived assuming the following full model dynamics, extending the model introduced for a single joint by Hashimoto [37] where feedforward compensation using desired torque is presented for torque control using harmonic drive built-in torque sensor. The JTFC2 model differs from (9) since has no damping contribution of the elastic transmission and external forces.

The basic control law used in [37] can be generalized in case of multi-joint robot. Thus using the same notation and conditions of (24), the control law  $\mathbf{u}_f$  can be written as a function of desired torque, where for  $\mathbf{u}_g$  is used (22):

$$\mathbf{u}_f = - \underbrace{\mathbf{I}_i^{-1} \mathbf{I}_m \boldsymbol{\tau}_s^D}_{\text{desired torque}} - \underbrace{\mathbf{I}_m \mathbf{K}_t^{-1} (\ddot{\boldsymbol{\tau}}_s^D - \mathbf{K}_d \dot{\mathbf{e}} - \mathbf{K}_p \mathbf{e})}_{\text{state feedback}} \quad (27)$$

The modified dynamics with the control law (27), leads to the following error dynamics equation:

$$\begin{aligned} & \mathbf{K}_t \bar{\mathbf{M}}^{-1} \mathbf{J}^T \mathbf{F}_l + \mathbf{B}_m \mathbf{D} \dot{\boldsymbol{\theta}}_m - \mathbf{K}_t \mathbf{I}_m^{-1} \boldsymbol{\tau}_d \\ &= \ddot{\mathbf{e}} + (\mathbf{K}_d + \mathbf{I}_i^{-1} \mathbf{C}_t) \dot{\mathbf{e}} + (\mathbf{K}_p + \mathbf{I}_i^{-1} \mathbf{K}_t) \mathbf{e} \end{aligned}$$

#### D. A passivity-based feedback controller (JTFC3)

The passivity-based state feedback is derived assuming the following full model dynamics (introduced by Ott in [38]), that differs from (9) for the absence of the motor's viscous friction term  $\mathbf{B}_m \mathbf{D} \dot{\boldsymbol{\theta}}_m$ .

In [38] the control law  $\mathbf{u}$  is designed as in (21) where  $\mathbf{u}_g$  are the torques due to the gravity, while the controller input  $\mathbf{u}_f$  can optimize the matching with a desired impedance  $\mathbf{I}_\theta$ , based on which the term  $\mathbf{u}_f$  after some algebraic transformations can be written as:

$$\mathbf{u}_f = - \underbrace{\mathbf{I}_m \mathbf{I}_\theta^{-1} \boldsymbol{\tau}_s^D}_{\text{desired torque}} - \underbrace{(\mathbf{I} - \mathbf{I}_m \mathbf{I}_\theta^{-1})(\boldsymbol{\tau}_s + \mathbf{C}_t \mathbf{K}_t^{-1} \dot{\boldsymbol{\tau}}_s)}_{\text{state feedback}} \quad (28)$$

So that the modified dynamics adopting the above control law leads to the following error dynamics equations where the error convergence can be set according to the selected value for  $\mathbf{I}_\theta$ :

$$\begin{aligned} & \mathbf{K}_t \bar{\mathbf{M}}^{-1} (-\boldsymbol{\tau}_s^D + \mathbf{J}^T \mathbf{F}_l) + \\ & + \mathbf{B}_m \mathbf{D} \dot{\boldsymbol{\theta}}_m - \mathbf{K}_t \mathbf{I}_m^{-1} \boldsymbol{\tau}_d = \\ & \ddot{\mathbf{e}} + \mathbf{C}_t (\mathbf{I}_\theta^{-1} + \bar{\mathbf{M}}^{-1}) \dot{\mathbf{e}} + \mathbf{K}_t (\mathbf{I}_\theta^{-1} + \bar{\mathbf{M}}^{-1}) \mathbf{e} \end{aligned}$$

#### E. Haptic rendering

The three torque control laws are used as inner feedback loop of the impedance control used to test the exoskeleton in the haptic rendering task. The desired end-effector force  $F_{ee}^D$  is due to the interaction with the virtual environment impedance. More in detail, the desired force is defined by:

$$\begin{cases} \mathbf{F}_{ee}^D = 0, & x < x_d \\ \mathbf{F}_{ee}^D = \mathbf{K}_x(x - x_d) - \mathbf{D}_x \dot{x}, & x \geq x_d \end{cases} \quad (29)$$

where  $x$  is the coordinate along the normal axis to the surface,  $x_d$  is the wall coordinate,  $\mathbf{K}_x$  and  $\mathbf{D}_x$  are the desired stiffness and damping respectively of the simulated virtual environment.

### V. EXPERIMENTS AND RESULTS

The performance of the torque and impedance controllers were assessed by experimental tests both in terms of *transparency* and *haptic rendering* performance measures. The tests show how the torque controls behave in constant and varying desired torque tracking. The first one is the transparency test in which the robot tries to keep the joint torque at zero Nm

while the user is moving the exoskeleton. The second test is the haptic rendering with a slanted flat surface with different simulated stiffness. More details on each test are reported in the subsections below.

The implemented control laws (22), (27) and (28) have been set using the model parameters. The proportional and derivative PD gains ( $K_p$  and  $K_d$ ) have been chosen to obtain a desired error dynamics, specifically the form that guarantees the minimum ITAE index. Notice that the control laws (22) and (27) have two degrees of freedom, i.e.  $K_p$  and  $K_d$  can be independently chosen, whereas the control law (28) exhibits only one degree of freedom, thus the two control gains are linked and they are calculated as a function of the desired inertia  $I_\theta$ .

#### A. Transparency

For the transparency test, a performance measurements was adopted based on multi-joint transparency as in [4] were the pHRI torque on each joint has been analyzed. More in detail, two kinds of trials have been done. The first type of trial uses the JTFC1 control law described in the subsection IV-B in order to verify how much the dynamics compensations improve the desired torque tracking. The second type of trials compare the three control laws and its aim is to understand how the terms of the controllers are related to the desired torque tracking.

The transparency tests were performed recruiting 10 healthy subjects (males, 8 right-handed) with a mean age:  $30.9 \pm 5.2$  years. All subjects were asked to sign a written informed consent for participating to the study.

The two transparency tests have a slightly difference: in the first trials the user moves the exoskeleton with no constraints, grabbing the end-effector handle (interaction forces are exerted only at the end-effector). Whereas, during the second transparency test, the user is linked with the exoskeleton at 2 anchor points at the arm and the forearm (by grasping the end-effector handle). An additional force sensor was mounted on the end-effector of the exoskeleton to measure the actual forces  $\mathbf{F}_h^*$  applied by the user at the handle interface.

As transparency index we evaluated the mean absolute pHRI torque and the mean peak absolute pHRI torque as in [4]. The measured end-effector forces provides only a qualitative index in the transparency test when a multi-contact interaction with the exoskeleton occurs. Conversely, the measured end effector norm force have been used to quantitative evaluate the controller performances during single-contact interactions.

1) *How dynamic compensation affects the transparency:* In order to understand how the dynamic compensation affects the transparency the scheme of figure 9 has been implemented using the JTFC1 control law plus the dynamics terms multiplied by  $\alpha$ , with  $0 \leq \alpha \leq 1$ .

In this test, the subject is asked to perform sinusoidal movements at each joint with a range of  $10 \text{ deg} \simeq 0.2 \text{ rad}$  with a frequency of  $0.5 \text{ Hz}$ , thus similar acceleration are imprinted to the exoskeleton joint for both “dynamic compensation” and “no compensation conditions”.

The experimental results for torque tracking, with a desired torque  $\boldsymbol{\tau}_s^D = \mathbf{0}$ , are shown for the second joint  $J_2$  in Fig. 10,

that is the joint with the highest link inertia. The control was set to follow his movement at zero-torque with (Fig. 10, left) and without (Fig. 10, right) dynamics compensation.

The upper plots show the joint position (black solid line), the central plots display the estimated acceleration (gray dashed line), to demonstrate the movements were similar in both cases. The lower plots represent the interaction torques estimated by the observer (gray dashed line) and measured by the force sensor (black solid line). Even if the estimated torques are similar in both cases, with dynamics compensation the actual interaction forces are lower, demonstrating that torque tracking is more precise and the user has to compensate less for the link dynamics.

2) *Comparison between the three torque controllers JTFC1, JTFC2 and JTFC3*: For this kind of trials the three joint torque controls presented in the section IV were tested with a desired torque set to zero ( $\tau_s^D = 0$ ). The tests were conducted as in [4]: the participants were asked to track a reference point on a circular path, displayed on a screen, with the end-effector parallel to the coronal plane in front of them. Figure 11 shows a subject while performing the transparency task. The diameter of the circle was equal to 0.3 m and the center position was set to the subject's chest height to move in a typical activities of daily living workspace. Circles have been performed at two speed levels: slow ( $45 \frac{deg}{s}$ ) and fast ( $90 \frac{deg}{s}$ ) in accordance with [4]. 10 repetitions for each speed level. Moreover, the sequence of the controllers was randomly assigned to each participant to mitigate potential order effects.

The comparative multi-joint transparency study is depicted in Fig. 13 whereas the real trajectories performed by a representative subject can be shown in the Fig. 12.

Fig. 13 shows that the full-state feedback controller (JTFC1) had the lowest mean torque and mean peak torque in the slow scenario and is more transparent respect to JTFC2 and JTFC3 in terms of interaction torques. Data were statistically compared with a paired t-test ( $\alpha = 0.05$ ) between the JTFC1 and JTFC2 conditions, and JTFC1 and JTFC3 conditions. Outliers were removed before any further analysis using a Thompson Tau test. The obtained mean torque results are statistically significant ( $p < 0.01$ ) for joints J1, J2 and J4 in both slow and fast conditions. The joint J3 implements the same PD feedback control in all the experiments and it performs equally in all speed and controllers conditions. The obtained results for JTFC1 are comparable with ones presented in [4] and are reported in detail in TABLE VI.

The control JTFC1 that implements a full-state feedback control performs better because it models in a more accurate and general way the joint dynamics. Moreover, the control

JTFC1 compensates for the modeled effects. Notice that, at joint level, the control JTFC3 behaves more similar to JTFC1 rather than to the control JTFC2, in fact the torque errors of the control JTFC1 and JTFC3 seems to be correlated to the link inertia. Moreover, from the analysis of the control torque errors at the joints (Fig. 13), it can be seen that the control JTFC2 exhibits an average error that is independent from the link inertia. The torque error over link inertia ratio for the elbow joint is the highest.

For the sake of completeness, we reported measured end-effector position, joint torques and e.e. forces of a part of the transparency test in Fig. 14 that allows for qualitative analysis.

To complete the transparency analysis, we performed a *smoothness* analysis as proposed in equation 3 of [3]. It is a jerk metric, i.e. the average rate of change of acceleration during a movement. Large values of the smoothness index indicate that many corrections are made during the movement by the subject. The values of the smoothness index for the 3 controllers have been reported in TABLE VII. Differently from the mean torque index, the controller JTFC1 do not exhibit the lowest smoothness value. We suppose this result is related to the less damped behavior performed by the exoskeleton with JTFC1, whereas both JTFC2 and JTFC3 offer a "viscous-like" resistance to the user motion that help smoothing the e.e. trajectory.

### B. Haptic rendering

The implemented torque controls can be used to render the interaction forces exchanged with a virtual surface of a given stiffness and damping, acting as impedance controls. In these tests the contact forces at the end-effector are proportional to the penetration length of the end-effector into the virtual wall surface and to its speed. The force is then converted to desired torques at the joints by multiplying the equation defined in (29) by the transpose of the Jacobian, where the control commands (22), (27) and (28) have been used respectively for JTFC1, JTFC2 and JTFC3.

In the experiments the user grabs the exoskeleton only at the end effector without applying any other force on the links. In this way, the forces measured by the end-effector's force sensor have been used to evaluate the overall system performance since these forces are not involved for the torque control.

The rendering experiments were composed by four different type of trials as depicted in Fig. 15:

- T1** "Slide on surface" experiment with moderate forces;
- T2** "Slide on surface" experiment with high forces;
- T3** "Collision with a surface" experiment with moderate speed;

TABLE VI  
MEAN TORQUE AND MEAN PEAK TORQUE FOR JTFC1

	Speed	J1	J2	J3	J4
Mean torque [Nm]	Slow	0.54	0.77	0.57	0.39
	Fast	0.58	0.88	0.63	0.44
Mean peak torque [Nm]	Slow	1.35	2.05	1.07	0.93
	Fast	1.36	2.36	1.24	1.06

TABLE VII  
SMOOTHNESS INDEX FOR THE 3 CONTROLLERS

Speed	JTFC1	JTFC2	JTFC3
Slow	80.87	47.10	47.80
Fast	107.46	85.48	119.08

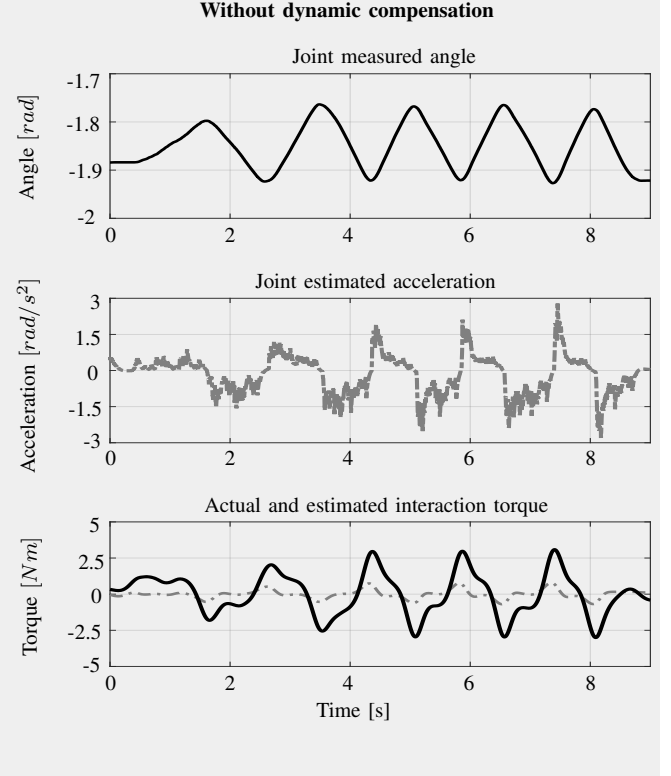
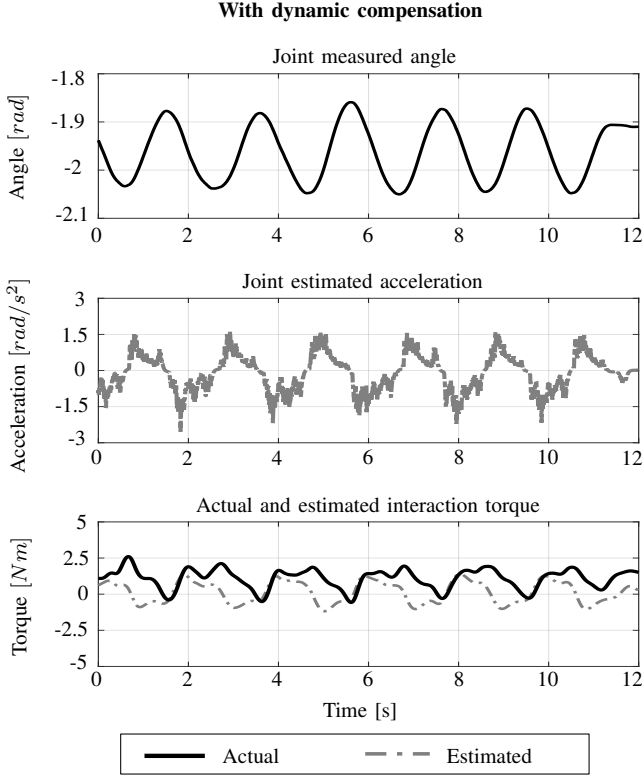


Fig. 10. Comparison between the estimated torque  $\tau_s$  and the actual torque that is calculated by force sensor for joint  $J_2$  (third row). Experiment was carried out providing dynamics compensation (left side) and without dynamics compensation (right side, in gray). For the two conditions, angular position and acceleration are reported in the first and second row respectively. Without dynamics compensations, the actual torques differs from the estimated ones resulting in a loss of transparency.

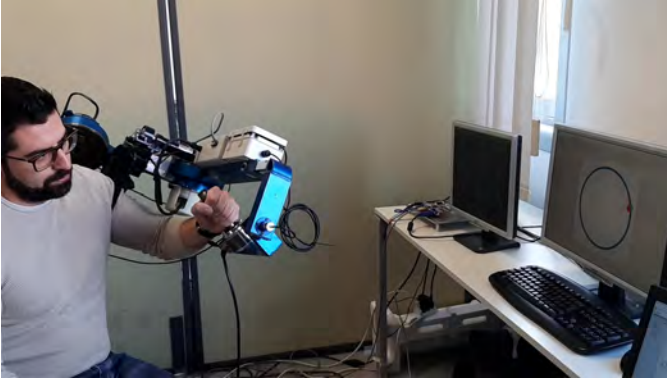


Fig. 11. Experimental setup of the transparency test. The user is linked to the exoskeleton at the shoulder level and at the end-effector (it grabs the handle). The user's elbow and the exoskeleton's one enter in contact during the trial execution. The subject moved the exoskeleton performing a circular trajectory at constant angular speed which reference is shown on a screen.

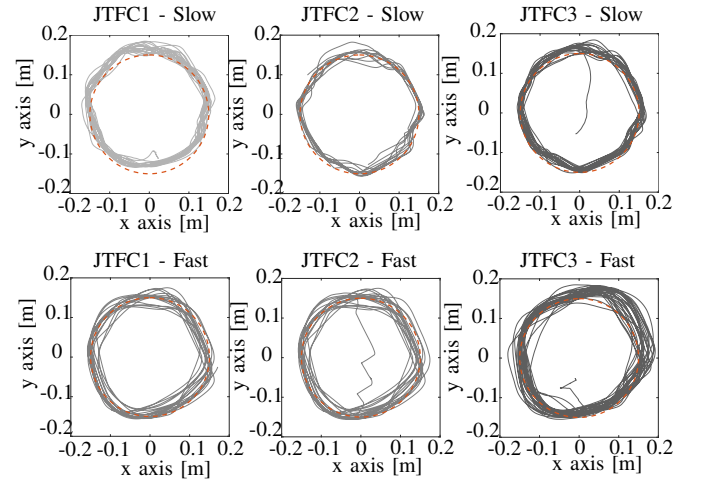


Fig. 12. The trajectories performed during the transparency test using the three control laws in the slow (first row) and fast (second row) conditions.

#### T4 "Collision with a surface" experiment with high speed.

During the T1 and T2 trials the experimenter slid the end-effector on the surface without sudden variations of penetration. The difference between the T1 and T2 trials is the average level of force along the orthogonal axes at the surface. In the T3 and T4 trials the aim is to test the dynamic performance of the controls, so the experimenter pushed the end-effector

on the surface. The difference between the T3 and T4 trials is the average slope of the desired force profiles. The 4 tests have been evaluated for each controls and with three different environment parameters, in order to consider a low, an intermediate and a high stiff wall.

The TABLE VIII reports the three environment parameters, the average forces involved in the T1 and T2 trials, the average force peaks and the average slope of the T3 and T4 trials.

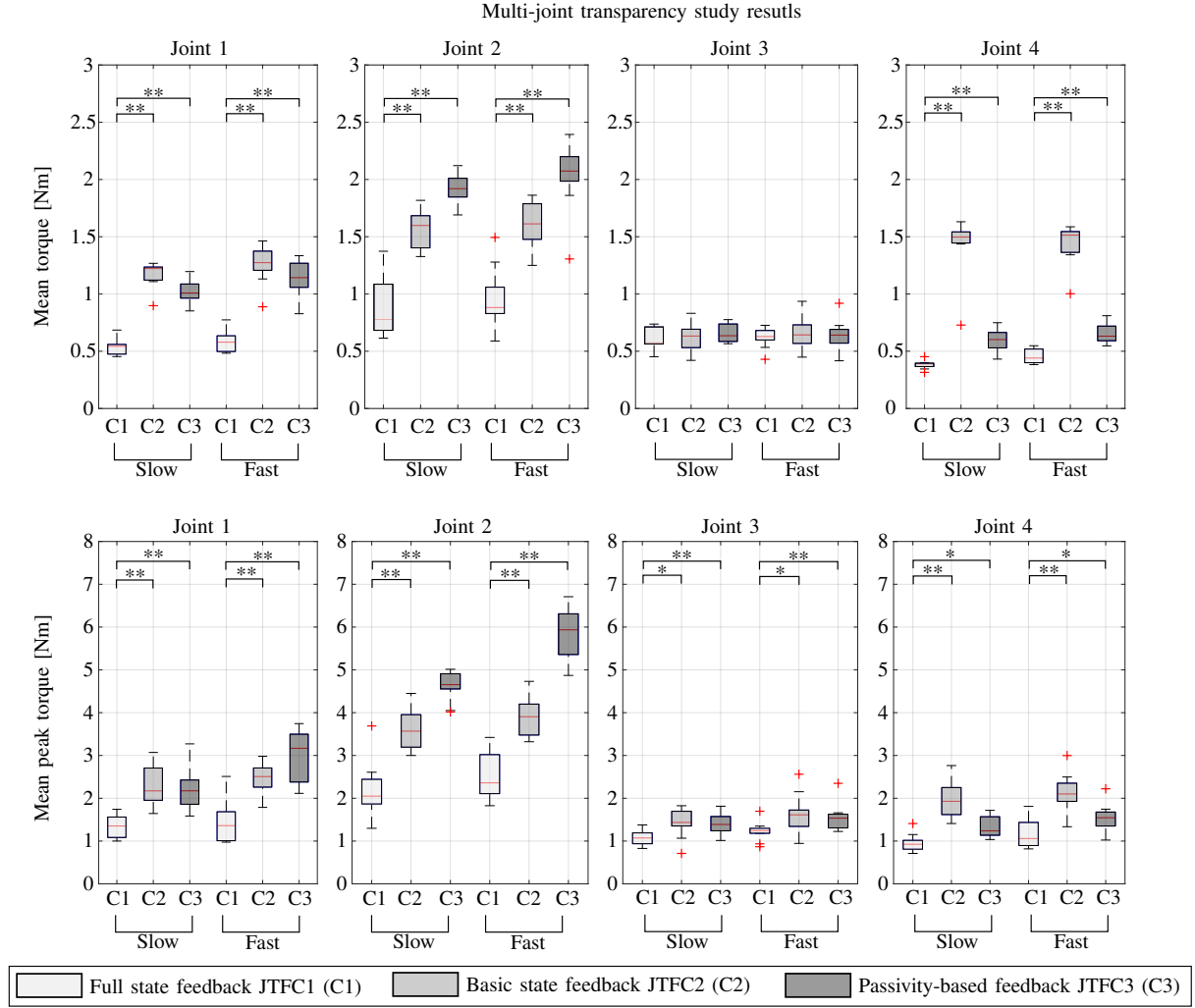


Fig. 13. Multi-joint transparency study. Mean absolute torque and mean absolute peak torque for the four Rehab-Exos actuated joints for the 10 subjects visualized as boxplots. The interaction torques have been evaluated for the 3 controllers in slow ( $45 \frac{deg}{s}$ ) and fast ( $90 \frac{deg}{s}$ ) speed conditions as proposed in [4]. JTFC1 offered the lowest resistive torque in both conditions for all the joints with high statistical significance (\*\*\*,  $p < 0.01$ ).

TABLE VIII  
THE AVERAGE FORCES INVOLVED IN THE T1 AND T2 TRIALS, THE AVERAGE FORCE PEAKS AND THE AVERAGE SLOPE OF THE T3 AND T4 TRIALS.

Env. Params.	T1	T2	T3	T4
5 kN/m	22.22 N	50.79 N	83.33 N	112.33 N
2 Ns/m	-	-	127.28 N/s	518.49 N/s
20 kN/m	22.81 N	66.14 N	103.97 N	136.97 N
7 Ns/m	-	-	159.25 N/s	550.99 N/s
40 kN/m	24.98 N	59.37 N	88.32 N	126.20 N
10 Ns/m	-	-	120.39 N/s	616.03 N/s

To evaluate the performances of the three different torque controls three indexes have been proposed, i.e.

- the mean of the norm of the error force vectors;
- the mean of the absolute value of the error of the orthogonal component;
- the mean of the angle between the desired forces and the measured ones.

The results can be shown in the Fig. 16. The first graph shows the average difference between the rendered forces by the controls and the desired forces with an aggregate index, i.e. the norm of the error vector. From this graph the reader can see that in all the condition the JTFC1 control performs better than the others, in fact the mean of the error is around 10 N in all the three cases.

To decompose the informations given in the first graph, other two indexes are considered, that are the average error of the orthogonal component of the force and the angle between the desired and the rendered forces. Unlike the norm of the error vector, these two indexes give information on the amplitude and the direction of the undesired force components. The second graph highlights that the JTFC1 control leads to an average error of 5 N along the task direction independently from the environment parameters, that is a good result coupled with the exhibited stable contact with the surface in every condition. The third graph is substantially in agreement with the previous ones.



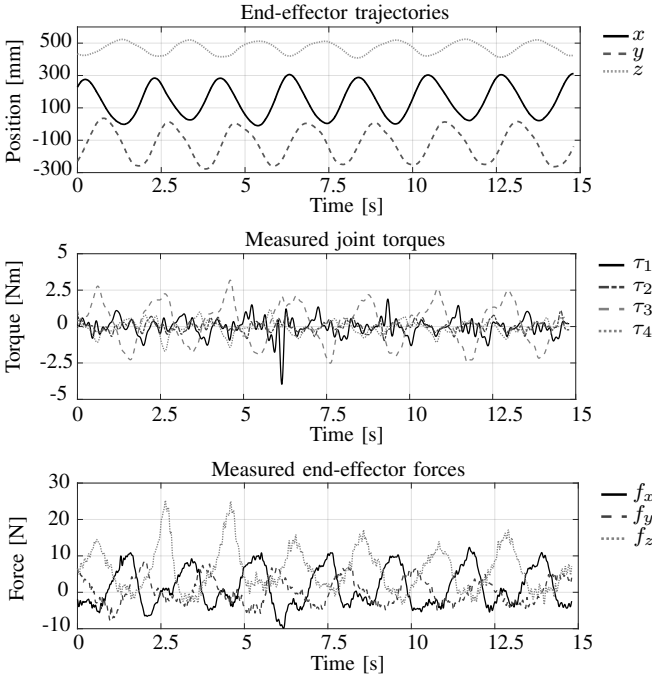


Fig. 14. An extract of the result of the transparency test using the JTFC1 controller. The user is not hindered by performing a circular trajectory in the XY plane (the  $z$  coordinate has a small variation compared to the  $x$  and  $y$  axis) at constant speed (first row). The joint torques (second row) are small compared to the maximum torque that can be exerted by the joints and only the  $J_3$  torque (the dashed gray line) exhibits a sinusoidal evolution. The third row plot reports the forces measured at the end-effector that are always smaller than 25 N.

## VI. DISCUSSION

The results highlight the advantages of using a full-state feedback controller that compensates also for estimated disturbance torques and for viscous torque losses of the motor. The major benefit on the use of the full state feedback control is high exhibited transparency during the free motion task. This means that the exoskeleton can affect less the user desired motion and at the same time the robot is able to more accurately identify the user intention (the human forces/torques).

Although the basic state feedback control (JTFC2) presents an average force modulus at the end-effector similar to the passivity-based feedback control (JTFC3), it hinders the user voluntary motion more than the other controls do. In fact the end-effector trajectory due to the control JTFC2 is the farthest from the desired one. This is because the JTFC1 and the JTFC3 take into account (although different ways) both the link's inertia and the motor's inertia, whereas the JTFC2 control considers only the motor's inertia. The full state controller explicitly estimates the load torques and feed-forwards this contribution by multiplying it by a gain. On the other side, the passivity-based controller imposes by control the desired link's inertia, thus this is a direct objective of the control.

The high transparency (the average force modulus at the end-effector is less than 6 N for JTFC1) is also due to the effect of the dynamic compensations. A correct estimation

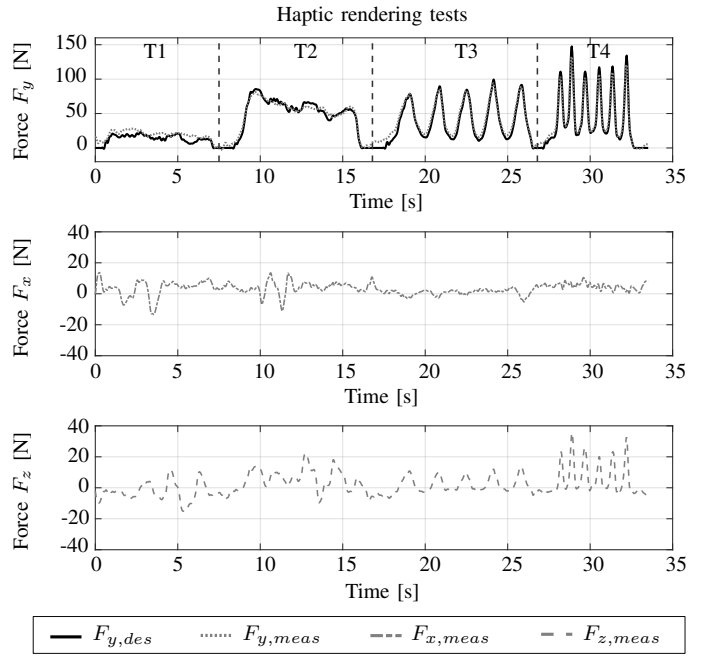


Fig. 15. The four trial types during an haptic rendering test. The desired forces  $F_{y,des}$  are plotted with black solid line whereas the measured orthogonal forces  $F_{y,meas}$  are plotted with gray dotted line in the first row. The two tangential components  $F_{x,meas}$  and  $F_{z,meas}$  are shown in the second and third rows respectively.

of the joint acceleration is crucial to obtain a transparency enhancement. This is the reason why the dynamic contributions are weighted by a constant less than 1. In fact only with a perfect acceleration estimation, a high transparency can be obtained exhibiting a stable behavior. The proposed methodology for the estimation of the acceleration through torque sensor data and motor data can help to improve the acceleration estimation.

An important result is the wide range of stable impedances that the system is capable of rendering. The Rehab-Exos was able to render a flat surface with a stiffness equal to 40 kN/m with all the three compared control laws with different performance but still preserving stability. This is certainly due to inherent mechanical damping of the system.

The mechanical design of the exoskeleton influences its performance. The residual torques at the joint are basically the effects of unmodeled link inertia and joint friction. A lighter design obtained with smaller motors and lower transmission ratio will lead to a more backdrivable solution at the cost of a less torque available at the joint. This could be a trade-off solution to achieve a more transparent device. Last but not least the torque sensor requires a more robust design; more in detail, to obtain a smaller sensitivity to non-axial loads a spoke with wider beams can be implemented.

The choice of a joint with an active impedance by control based on a torque sensor presents a valid alternative to the passive inherent compliant actuators in order to achieve a more compact and simpler mechanics and electronics. The proposed torque control combined with the joint mechanics allow building safe and responsive control strategies suitable

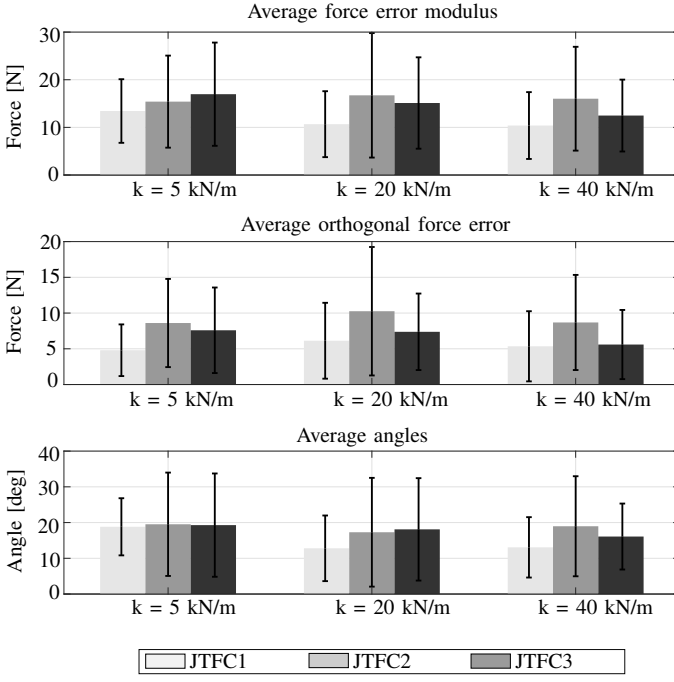


Fig. 16. In the first row, the average of the modulus of the error force vectors at the end effector of the 3 controllers in the rendering task. For this test, 3 stiffness has been evaluated: 5kN/m (small), 20 kN/m (medium) and 40 kN/m (high). In the second row, the average error forces of the orthogonal component. In the third row, the average angle between the desired force vectors and the measured ones.

for rehabilitation and assistance.

## VII. CONCLUSION

This paper presents the Rehab-Exos exoskeleton design and in particular the design of the joint torque sensors based on strain gauges. Some sensor's issue have been explained and two possible hypotheses have been proposed. Then an interaction torque control has been developed and validated by experimental tests such as the transparency test and the haptic interaction tasks. The kinematics and dynamics of the device are calculated by a full dynamics model implemented in a centralized torque control. The torque tracking for each joint is performed by single-joint full-state Kalman filter and a torque feedback controller. The centralized control provides to each single-joint observer the desired torque for force feedback and an estimation of the joint torques due to links dynamic loads to be compensated by the control as feed-forward contributions. The developed full-state feedback control was then compared with a basic feedback control and a passivity-based feedback control. Results show how the full-state approach is effective for estimating the human interaction force cleaned up of the inertial and gravity contributions due to the non negligible mechanical properties of the exoskeleton structure. The full-state feedback control is more accurate and transparent than the other two controls. The proposed control strategy combined with the presence of a joint torque sensor can enhance the performances of the human-robot interaction based on exoskeleton even in the presence of non backdrivability.

## ACKNOWLEDGMENTS

The authors would like to thank Marco Graffiedi for his contribute on the study of the torque sensor cross-talk reading.

## VIII. APPENDIX I

Let us study the effect under static condition of the application of a motor torque compensating for the non-linearity due to gravity, estimated as  $\hat{\mathbf{G}}(\mathbf{D}\hat{\boldsymbol{\theta}}_m)$ , with:

$$\boldsymbol{\tau}_m = \hat{\mathbf{G}}(\mathbf{D}\hat{\boldsymbol{\theta}}_m) + \mathbf{u} \quad (30)$$

where  $\mathbf{u}$  represents the actual control command. Under static conditions it can be found that:

$$\mathbf{u} = -\mathbf{J}^T \mathbf{F}_h + \mathbf{G}(\boldsymbol{\theta}) - \hat{\mathbf{G}}(\mathbf{D}\hat{\boldsymbol{\theta}}_m) \simeq -\mathbf{J}^T \mathbf{F}_h \quad (31)$$

since  $\hat{\mathbf{G}}(\mathbf{D}\hat{\boldsymbol{\theta}}_m) \simeq \mathbf{G}(\boldsymbol{\theta})$ . Under dynamic conditions, the incomplete cancellation of the gravity component due to the elasticity of the joint transmission can be modeled by introducing a disturbance term  $\delta\mathbf{g} = \mathbf{G}(\boldsymbol{\theta}) - \hat{\mathbf{G}}(\mathbf{D}\hat{\boldsymbol{\theta}}_m)$ , that can be summed up to  $\mathbf{F}_h$  as a disturbance noise supported by the operator.

So a variable apparent dynamic force  $\mathbf{F}_{dyn}$  can be defined such that  $\mathbf{J}^T \Delta \mathbf{F}_{dyn}(\dot{\boldsymbol{\theta}}, \boldsymbol{\theta}) = -\Delta \mathbf{M}(\boldsymbol{\theta})\dot{\boldsymbol{\theta}} - \mathbf{C}(\dot{\boldsymbol{\theta}}, \boldsymbol{\theta})\dot{\boldsymbol{\theta}}$ . The new variable  $\Delta \mathbf{F}_{dyn}$ , representing uncompensated and/or unmodeled dynamics, can be considered as a disturbance force and considered as a contribution term to the overall external load force  $\mathbf{F}_1$  expressed by:

$$\mathbf{F}_1 = \underbrace{\mathbf{F}_h}_{\text{exogenous}} + \underbrace{\delta\mathbf{g} + \Delta \mathbf{F}_{dyn}}_{\text{endogenous}} \quad (32)$$

This in general states that the external forces are the sum of exogenous  $\mathbf{F}_h$  and endogenous inputs  $\delta\mathbf{g} + \Delta \mathbf{F}_{dyn}$ . While exogenous inputs are unknown a priori and depending on human operator behavior, endogenous inputs can be estimated and compensated to some extent.

So introducing the variable substitution expressed by (11), dynamic equations can be reformulated as follow:

$$\mathbf{I}_m \mathbf{D}\ddot{\boldsymbol{\theta}}_m + \mathbf{B}_m \mathbf{D}\dot{\boldsymbol{\theta}}_m + \mathbf{C}_t \mathbf{K}_t^{-1} \dot{\boldsymbol{\tau}}_s + \boldsymbol{\tau}_s + \mathbf{u} + \boldsymbol{\tau}_d \quad (33)$$

$$\bar{\mathbf{M}}\ddot{\boldsymbol{\theta}} + \mathbf{C}_t \mathbf{K}_t^{-1} \dot{\boldsymbol{\tau}}_s + \boldsymbol{\tau}_s = \mathbf{J}^T \mathbf{F}_1 \quad (34)$$

But we know that

$$\mathbf{K}_t^{-1} \dot{\boldsymbol{\tau}}_s + \mathbf{D}\ddot{\boldsymbol{\theta}}_m = \ddot{\boldsymbol{\theta}} \quad (35)$$

Then making substitution of (35) in (34) to eliminate  $\ddot{\boldsymbol{\theta}}$ , we obtain:

$$\bar{\mathbf{M}}\mathbf{D}\ddot{\boldsymbol{\theta}}_m + \bar{\mathbf{M}}\mathbf{K}_t^{-1} \ddot{\boldsymbol{\tau}}_s + \mathbf{C}_t \mathbf{K}_t^{-1} \dot{\boldsymbol{\tau}}_s + \boldsymbol{\tau}_s = \mathbf{J}^T \mathbf{F}_l \quad (36)$$

and then replacing from (33)  $\mathbf{D}\ddot{\boldsymbol{\theta}}_m = \mathbf{I}_m^{-1} \{-\mathbf{B}_m \mathbf{D}\dot{\boldsymbol{\theta}}_m + \mathbf{C}_t \mathbf{K}_t^{-1} \dot{\boldsymbol{\tau}}_s + \boldsymbol{\tau}_s + \mathbf{u} + \boldsymbol{\tau}_d\}$  and defining  $\mathbf{I}_i^{-1} = \bar{\mathbf{M}}^{-1} + \mathbf{I}_m^{-1}$ , dynamics equations can be put in the following form:

$$\ddot{\tau}_s + \mathbf{C}_t \mathbf{I}_i^{-1} \dot{\tau}_s + \mathbf{K}_t \mathbf{I}_i^{-1} \tau_s = \mathbf{K}_t \bar{\mathbf{M}}^{-1} \mathbf{J}^T \mathbf{F}_1 + \mathbf{K}_t \mathbf{I}_m^{-1} (\mathbf{B}_m \mathbf{D} \dot{\mathbf{m}} - \boldsymbol{\tau}_d - \mathbf{u}) \quad (37)$$

This form of the dynamics equation is useful for defining a full-state feedback control law and an optimal observer for the estimation of joint torque.

## REFERENCES

- [1] A. Frisoli, *Wearable Robots*. Berlin, Heidelberg: Springer Berlin Heidelberg, 2019, pp. 1–8. [Online]. Available: [https://doi.org/10.1007/978-3-642-41610-1\\_22-1](https://doi.org/10.1007/978-3-642-41610-1_22-1)
- [2] A. Bajcsy, D. P. Losey, M. K. O'Malley, and A. D. Dragan, "Learning robot objectives from physical human interaction," *Proceedings of Machine Learning Research*, vol. 78, pp. 217–226, 2017.
- [3] N. Jarrasse, M. Tagliabue, J. V. Robertson, A. Maiza, V. Crocher, A. Roby-Brami, and G. Morel, "A methodology to quantify alterations in human upper limb movement during co-manipulation with an exoskeleton," *IEEE Transactions on neural systems and Rehabilitation Engineering*, vol. 18, no. 4, pp. 389–397, 2010.
- [4] F. Just, Ö. Özgen, P. Bösch, H. Bobrovsky, V. Klamroth-Marganska, R. Riener, and G. Rauter, "Exoskeleton transparency: feed-forward compensation vs. disturbance observer," *at-Automatisierungstechnik*, vol. 66, no. 12, pp. 1014–1026, 2018.
- [5] J. E. Colgate and J. M. Brown, "Factors affecting the z-width of a haptic display," in *Proceedings of the 1994 IEEE International Conference on Robotics and Automation*. IEEE, 1994, pp. 3205–3210.
- [6] N. Diolaiti, G. Niemeyer, F. Barbagli, and J. K. Salisbury, "A criterion for the passivity of haptic devices," in *Proceedings of the 2005 IEEE International Conference on Robotics and Automation*. IEEE, 2005, pp. 2452–2457.
- [7] H. S. Lo and S. Q. Xie, "Exoskeleton robots for upper-limb rehabilitation: State of the art and future prospects," *Medical engineering & physics*, vol. 34, no. 3, pp. 261–268, 2012.
- [8] E. Pirondini, M. Coscia, S. Marcheschi, G. Roas, F. Salsedo, A. Frisoli, M. Bergamasco, and S. Micera, "Evaluation of the effects of the arm light exoskeleton on movement execution and muscle activities: a pilot study on healthy subjects," *Journal of neuroengineering and rehabilitation*, vol. 13, no. 1, p. 1, 2016.
- [9] M. Xiloyannis, D. Chiaradia, A. Frisoli, and L. Masia, "Physiological and kinematic effects of a soft exosuit on arm movements," *Journal of neuroengineering and rehabilitation*, vol. 16, no. 1, p. 29, 2019.
- [10] M. J. Kim, W. Lee, J. Y. Choi, Y. S. Park, S. H. Park, G. Chung, K.-L. Han, I. S. Choi, I. H. Suh, Y. Choi *et al.*, "Powered upper-limb control using passivity-based nonlinear disturbance observer for unknown payload carrying applications," in *Robotics and Automation (ICRA), 2016 IEEE International Conference on*. IEEE, 2016, pp. 2340–2346.
- [11] D. Buongiorno, E. Sotgiu, D. Leonardi, S. Marcheschi, M. Solazzi, and A. Frisoli, "Wres: a novel 3dof wrist exoskeleton with tendon-driven differential transmission for neuro-rehabilitation and teleoperation," *IEEE Robotics and Automation Letters*, 2018.
- [12] J. Rebelo, T. Sednaoui, E. B. den Exter, T. Krueger, and A. Schiele, "Bilateral robot teleoperation: A wearable arm exoskeleton featuring an intuitive user interface," *IEEE Robotics & Automation Magazine*, vol. 21, no. 4, pp. 62–69, 2014.
- [13] D. Buongiorno, D. Chiaradia, S. Marcheschi, M. Solazzi, and A. Frisoli, "Multi-dofs exoskeleton-based bilateral teleoperation with the time-domain passivity approach," *Robotica*, vol. 37, no. 9, p. 1641–1662, 2019.
- [14] M. Mihelj, T. Nef, and R. Riener, "Armin ii-7 dof rehabilitation robot: mechanics and kinematics," in *Robotics and Automation, 2007 IEEE International Conference on*. IEEE, 2007, pp. 4120–4125.
- [15] R. Verthey, A. Frisoli, A. Dettori, M. Solazzi, and M. Bergamasco, "Development of a new exoskeleton for upper limb rehabilitation," in *Rehabilitation Robotics, 2009. ICORR 2009. IEEE International Conference on*. IEEE, 2009, pp. 188–193.
- [16] C. Carignan, M. Liszka, and S. Roderick, "Design of an arm exoskeleton with scapula motion for shoulder rehabilitation," in *Advanced Robotics, 2005. ICAR'05. Proceedings., 12th International Conference on*. IEEE, 2005, pp. 524–531.
- [17] A. Frisoli, F. Salsedo, M. Bergamasco, B. Rossi, and M. Carboncini, "A force-feedback exoskeleton for upper-limb rehabilitation in virtual reality," *Applied Bionics and Biomechanics*, vol. 6, no. 2, pp. 115–126, 2009.
- [18] J. C. Perry, J. Rosen, and S. Burns, "Upper-limb powered exoskeleton design," *Mechatronics, IEEE/ASME Transactions on*, vol. 12, no. 4, pp. 408–417, 2007.
- [19] P. Garrec, J. Fricconneau, Y. Measson, and Y. Perrot, "Able, an innovative transparent exoskeleton for the upper-limb," in *Intelligent Robots and Systems, 2008. IROS 2008. IEEE/RSJ International Conference on*. IEEE, 2008, pp. 1483–1488.
- [20] L. Tiseni, M. Xiloyannis, D. Chiaradia, N. Lotti, M. Solazzi, H. van der Kooij, A. Frisoli, and L. Masia, "On the edge between soft and rigid: an assistive shoulder exoskeleton with hyper-redundant kinematics," in *2019 IEEE 16th International Conference on Rehabilitation Robotics (ICORR)*, June 2019, pp. 618–624.
- [21] N. G. Tsagarakis and D. G. Caldwell, "Development and control of a soft-actuated exoskeleton for use in physiotherapy and training," *Autonomous Robots*, vol. 15, no. 1, pp. 21–33, 2003.
- [22] J. Klein, S. Spencer, J. Allington, J. E. Bobrow, and D. J. Reinkensmeyer, "Optimization of a parallel shoulder mechanism to achieve a high-force, low-mass, robotic-arm exoskeleton," *Robotics, IEEE Transactions on*, vol. 26, no. 4, pp. 710–715, 2010.
- [23] B. Vanderborght, A. Albu-Schäffer, A. Bicchi, E. Burdet, D. G. Caldwell, R. Carloni, M. Catalano, O. Eiberger, W. Friedl, G. Ganesh *et al.*, "Variable impedance actuators: A review," *Robotics and autonomous systems*, vol. 61, no. 12, pp. 1601–1614, 2013.
- [24] J. F. Veneman, R. Kruidhof, E. E. Hekman, R. Ekkelenkamp, E. H. Van Asseldonk, and H. Van Der Kooij, "Design and evaluation of the lopes exoskeleton robot for interactive gait rehabilitation," *IEEE Transactions on Neural Systems and Rehabilitation Engineering*, vol. 15, no. 3, pp. 379–386, 2007.
- [25] N. Vitiello, T. Lenzi, S. Roccella, S. M. M. De Rossi, E. Cattin, F. Giovacchini, F. Vecchi, and M. C. Carrozza, "Neuroexos: A powered elbow exoskeleton for physical rehabilitation," *IEEE Transactions on Robotics*, vol. 29, no. 1, pp. 220–235, 2013.
- [26] P. Cherelle, V. Grosu, P. Beyl, A. Mathys, R. Van Ham, M. Van Damme, B. Vanderborght, and D. Lefeber, "The macepa actuation system as torque actuator in the gait rehabilitation robot altacro," in *Biomedical Robotics and Biomechanics (BioRob), 2010 3rd IEEE RAS and EMBS International Conference on*. IEEE, 2010, pp. 27–32.
- [27] S. Wolf, O. Eiberger, and G. Hirzinger, "The dlr fsj: Energy based design of a variable stiffness joint," in *Robotics and Automation (ICRA), 2011 IEEE International Conference on*. IEEE, 2011, pp. 5082–5089.
- [28] J.-H. Kim, M. Shim, D. H. Ahn, B. J. Son, S.-Y. Kim, D. Y. Kim, Y. S. Baek, and B.-K. Cho, "Design of a knee exoskeleton using foot pressure and knee torque sensors," *International Journal of Advanced Robotic Systems*, vol. 12, no. 8, p. 112, 2015.
- [29] G. Aguirre-Ollinger, J. E. Colgate, M. A. Peshkin, and A. Goswami, "Design of an active one-degree-of-freedom lower-limb exoskeleton with inertia compensation," *The International Journal of Robotics Research*, vol. 30, no. 4, pp. 486–499, 2011.
- [30] B. Hwang and D. Jeon, "A method to accurately estimate the muscular torques of human wearing exoskeletons by torque sensors," *Sensors*, vol. 15, no. 4, pp. 8337–8357, 2015.
- [31] D. Zanotto, T. Lenzi, P. Stegall, and S. K. Agrawal, "Improving transparency of powered exoskeletons using force/torque sensors on the supporting cuffs," in *Rehabilitation Robotics (ICORR), 2013 IEEE International Conference on*. IEEE, 2013, pp. 1–6.
- [32] W. M. dos Santos, G. A. Caurin, and A. A. Siqueira, "Design and control of an active knee orthosis driven by a rotary series elastic actuator," *Control Engineering Practice*, vol. 58, pp. 307–318, 2017.
- [33] A. G. L. Junior, R. M. de Andrade, and A. Bento Filho, "Series elastic actuator: Design, analysis and comparison," in *Recent Advances in Robotic Systems*. InTech, 2016.
- [34] C. Lee and S. Oh, "Integrated transmission force estimation method for series elastic actuators," in *Advanced Motion Control (AMC), 2018 IEEE 15th International Workshop on*. IEEE, 2018, pp. 681–686.
- [35] A. G. Leal-Junior, A. Frizera, C. Marques, M. R. Sánchez, W. M. dos Santos, A. A. Siqueira, M. V. Segatto, and M. J. Pontes, "Polymer optical fiber for angle and torque measurements of a series elastic actuator's spring," *Journal of Lightwave Technology*, vol. 36, no. 9, pp. 1698–1705, 2018.
- [36] N. Kashiri, J. Malzahn, and N. G. Tsagarakis, "On the sensor design of torque controlled actuators: A comparison study of strain gauge and encoder-based principles," *IEEE Robotics and Automation Letters*, vol. 2, no. 2, pp. 1186–1194, 2017.

- [37] M. Hashimoto and Y. Kiyosawa, "Experimental study on torque control using harmonic drive built-in torque sensors," *Journal of Robotic Systems*, vol. 15, no. 8, pp. 435–445, 1998.
- [38] A. Kugi, C. Ott, A. Albu-Schaffer, and G. Hirzinger, "On the passivity-based impedance control of flexible joint robots," *Robotics, IEEE Transactions on*, vol. 24, no. 2, pp. 416–429, 2008.
- [39] R. Vertechy, A. Frisoli, M. Solazzi, D. Pellegrinetti, and M. Bergamasco, "An interaction-torque controller for robotic exoskeletons with flexible joints: Preliminary experimental results," in *Intelligent Robots and Systems (IROS), 2012 IEEE/RSJ International Conference on*. IEEE, 2012, pp. 335–340.



**Antonio Frisoli** (Eng., PhD) is Professor of Robotics and Mechanical Engineering at the Sant'Anna School of Advanced Studies, Pisa-Italy, where he is head of the Human-Robot Interaction area at PERCRO laboratory of TeCIP Institute. He received his PhD (2002) with honors in Industrial and Information Engineering from the Sant'Anna School of Advanced Studies, Italy and the MSc (1998) in Mechanical Engineering, minor Robotics, from University of Pisa-Italy. He has been chair of the IEEE Technical Committee on Haptics, the general chair of the Eurohaptics 2018 conference in Pisa and Human-Machine Interaction summer school HMISS 2017. In the field of robotics and haptics he acts as associated editor in numerous international conferences, such as IEEE Worldhaptics, IEEE Roman, IEEE Haptic Symposium among many others, and journals, such as IEEE Robotics and Automation Letters and MIT Press Presence.



**Domenico Chiaradia** received the B.S. and M.S. degrees with honours in control theory and automation engineering from the Polytechnic University of Bari, Italy, in 2011 and 2014 respectively. He is currently pursuing the Ph.D. degree in robotics engineering at Perceptual Robotics (PERCRO) Laboratory, TeCIP Institute, Sant'Anna School of Advanced Studies, Pisa, Italy. His research interest includes control of rigid and soft exoskeletons for assistance and rehabilitation, torque control, control of haptic interfaces and physical human-robot interaction.



**Massimiliano Solazzi** (Eng., Ph.D.) is Assistant Professor in Applied Mechanics at the Sant'Anna School of Advanced Studies in Pisa, Italy. He carries out his research at the Percro laboratory - TeCIP. In 2010 he received the PhD Degree in Innovative Technologies from the Sant'Anna School of Advanced Studies. His research interests concerns: the design of robotic interfaces for virtual reality, teleoperation and rehabilitations, and the psychophysical validation of HMI.



**Rocco Vertechy** (Eng., Ph.D.) is Associate Professor at the Industrial Engineering Department of the School of Engineering and Architecture of the University of Bologna in Italy, where he leads the group on advanced actuation technologies and renewable energy robotic systems. He is Mechanical Engineer (2001) and PhD in Mechanics of Machines (2005). He was: Research Assistant at the Department of Mechanical Engineering, University of Canterbury (New Zealand); Visiting Researcher at the Robotics Locomotion Laboratory, Stanford University (California);

Contract Professor at the University of Bologna; Assistant Professor at the Perceptual Robotics Laboratory of the Scuola Superiore Sant'Anna (Italy).